Report Title: Optimization of the Cathode Long-Term Stability in Molten Carbonate Fuel Cells: Experimental Study and Mathematical Modeling

Type of Report: Semiannual Progress Report

Reporting Period Start Date: April 1, 2001

Reporting Period End Date: September 30, 2001

Principal Author(s): Dr. Ralph E. White and Dr. Branko N. Popov

Date Report was Issued: October, 2001

DOE Award Number: DE-AC26-99FT40714 Modification A001

Name and Address of Submitting Organization:

Dr. Ralph E. White, Project Manager
Department of Chemical Engineering
University of South Carolina
Columbia, South Carolina 29208

DISCLAIMER

ABSTRACT

The dissolution of NiO cathodes during cell operation is a limiting factor to the successful commercialization of molten carbonate fuel cells (MCFCs). Lithium cobalt oxide coating onto the porous nickel electrode has been adopted to modify the conventional MCFC cathode which id believed to increase the stability of the cathodes in the carbonate melt. The material used for surface modification should possess thermodynamic stability in the molten carbonate and also should be electro catalytically active for MCFC reactions. Lithium Cobalt oxide was coated on Ni cathode by a sol-gel coating. The morphology and the $LiCoO_2$ formation of $LiCoO_2$ coated NiO was studied using scanning electron microscopy and X-Ray diffraction studies respectively. The electrochemical performance lithium cobalt oxide coated NiO cathodes were investigated with open circuit potential measurement and current-potential polarization studies. These results were compared to that of bare NiO. Dissolution of nickel into the molten carbonate melt was less in case of lithium cobalt oxide coated nickel cathodes. $LiCoO_2$ coated on the surface prevents the dissolution of Ni in the melt and thereby stabilizes the cathode. Finally, lithium cobalt oxide coated nickel shows similar polarization characteristics as nickel oxide.

Conventional theoretical models for the molten carbonate fuel cell cathode are based on the thin film agglomerate model. The principal deficiency of the agglomerate model, apart from the simplified pore structure assumed, is the lack of measured values for film thickness and agglomerate radius. Both these parameters cannot be estimated appropriately. Attempts to estimate the thickness of the film vary by two orders of magnitude. To avoid these problems a new three phase homogeneous model has been developed using the volume averaging technique. The model considers the potential and current variation in both liquid and solid phases. Using this approach, volume averaged concentrations of both gaseous and liquid phase reactants are obtained separately. The polarization characteristics of the electrode have been studied for different electrode parameters. The effect of different design parameters on the electrode performance has also been analyzed. Finally, the model has been used to analyze the impedance response of the MCFC cathode.

TABLE OF CONTENTS

LIST OF GRAPHICAL MATERIALS

LIST OF TABLES

INTRODUCTION

The Molten Carbonate Fuel cell (MCFC), operating at a temperature of 650°C, has been under intensive development for the last few decades as a second-generation fuel cell [1,2]. Significant advances have been done in addressing design issues resulting in the development of prototype MCFC power generators. However, several hurdles remain before commercialization of molten carbonate fuel cells can be realized. The primary challenge remains in the proper selection of materials for the cathode and current collector. Current state-of-art [3] relies on NiO cathodes fabricated from Ni powder. However, during cell operation, nickel oxide dissolves in the electrolyte [4] and does not satisfy long-term stability criteria (over 40,000 hours of operation [5] without replacement). Nickel oxide reacts with CO_2 present in the electrolyte according to an acidic dissolution mechanism.

$$\mathrm{NiO} + \mathrm{CO_2} \rightarrow \mathrm{Ni^{2+}} + \mathrm{CO_3}^{2-}$$

The dissolved nickel remains in equilibrium with the NiO cathode. Simultaneously, the Ni^{2+} cation diffuses to the anode side of the electrolyte and is then reduced in the hydrogen atmosphere to metallic nickel. The diffusion of Ni^{2+} cation fuels more dissolution of nickel from the cathode. Continued deposition of Ni in the anode region eventually leads to a short circuit between the anode and cathode. The dissolution is accelerated under higher CO_2 partial pressure and results in lowering the operating life of the cell. Apart from this, cathode dissolution results in loss of active material and in decrease of the active surface area available for the oxygen reduction reaction (cathodic reaction) leading to degradation in fuel cell performance.

Current state-of-art on solving the Ni dissolution problem is focused on varying the molten salt constituents [6,7] or using alternate cathode materials [8-10]. More basic molten carbonate melts such as Li/Na carbonate eutectic have been used to decrease the Ni dissolution rate in the melt [6,7]. Alkaline earth metal salts based on Ba or Sr have also been used as additives to increase the basicity of the melt. However, using more basic molten carbonate melts only partially solves the problem, since these melts decrease the NiO dissolution rate by 10 to 15% only [6,7].

The other approach to counter the nickel dissolution problem is to either modify NiO or to identify alternate cathode materials, which have longer life in the melt. Alternate electrodes should have good electronic conductivity, chemical stability and proper microstructure for use as MCFC cathodes. $LiFeO_2$ and $LiCoO_2$ offered initial promise as replacement material for NiO cathodes [8-10]. However, the exchange current density for oxygen reduction reaction on $LiFeO_2$ is about two orders of magnitude lower than that on NiO. Thus, the slow kinetics for oxygen reduction limits the possibilities for further improvement of cathodes based on this material. $LiCoO_2$ is more stable than NiO in alkaline environment [8]. However, $LiCoO_2$ is less electronically conductive than NiO and is more expensive than NiO. Other choices for cathode materials have failed on either one of these factors namely – low electronic conductivity and poor oxygen reduction kinetics. This being the case, surface modification of NiO with more resistant materials is being considered as the more viable alternative.

Based on previous investigations [11,12] cobalt has been chosen to modify the surface of the NiO cathode and reduce its dissolution. Fukui *et al* [11] and Zhang *et al* [12] studied the effect of cobalt coating on nickel oxide particles used as cathodes in MCFCs. Ni particles were covered with CoO particles mechanically. Composites made of the Ni-CoO particles showed better corrosion resistance as compared to that of conventional NiO in Li-K carbonate melt. However, polarization characteristics of the Ni-CoO composite were not shown. Recently, Kuk *et al* [13] prepared $LiCoO_2$ coated NiO electrodes using cobalt electroplating followed by oxidation in molten Li and K carbonate electrolyte. Materials chosen for modifying the NiO surface should not affect the performance of the MCFC cathode. $LiCoO_2$ layers were formed on the internal surface of porous NiO electrodes by a solution impregnation technique using lithium hydroxide and cobalt hydroxide dissolved in acetic acid [14]. Nam *et al* also report a sol-gel coating of $LiCoO_2$ on NiO using acrylic acid as a chelating agent [14]. Zhang et al adopted a solution dipping method for the formation of Ni/Co compound to increase the stability of MCFC cathodes [15]. In another approach Fukui *et al* coated cobalt oxide on to the Ni surface using a mechanofusion system to improve the cathode stability in molten alkali carbonate melt [16]. Earlier, micro-encapsulation of Co onto the porous nickel electrodes was carried out in our lab and it was evident from the results that this could be an alternate approach to fabricate a MCFC cathode material with enhanced stability in molten carbonate cathode working environment.

The MCFC cathode was stabilized by the electrodeposition of niobium onto nickel electrode followed by oxidation. It was found that under a cathode atm. of p(CO2)/p(O2) = 0.67 atm/0.33 atm, the equil. soly. of nickel ions in (Li0.62, K0.38)2CO3 melt at 650° C is about 17 ppm for the nickel oxide electrode and 8 ppm for the preoxidized nickel-niobium alloy electrode. The improvement in the stability of material in the melt may be attributed to the formation of a more dense nodular structure for the nickel-niobium alloy electrode when compared with a Ni electrode during pre-oxidation. As far as the thermal stability and the polarization performance are concerned, the pre-oxidized nickel-niobium alloy can be considered as a candidate for the cathode material of MCFCs [17]. The *in-situ* oxidation of Ni-5 at. % Al and Ni-15 at. %Al alloys in molten Li and K carbonate melt were investigated by Mohamedi *et al* [18]. The period of the oxidation process depends on the aluminum content in the alloy. Ni-5 at. % Al electrode exhibited excellent stability during one-week immersion in the carbonate melts. Extension of cathode lifetime in molten carbonate fuel cells (MCFC) appears possible if the Ni cathode is modified by the addition of small concentration of aluminum. Thin films of $LiCoO_2$ or $LiMg_{0.05}Co_{0.95}O_2$ were prepared on a cathode body by a Complex Sol-Gel Process in order to protect them against dissolution [19]. A 350 hundred hours test in molten carbonates proved that the cathode bodies covered with $LiCoO_2$ are completely prevented from dissolution of Ni in a molten K/Li electrolyte. Dissolution of $LiCoO_2$ coating was not observed as well.

Hence the objective of this study is to prepare and characterize $LiCoO_2$ coated NiO as a cathode material in molten carbonate fuel cells. For this, two different sol-gel methods, differing only in the complexing agent, were adopted to make $LiCoO_2$ coating onto the porous nickel electrodes. The sol-gel method was adopted since it yields ultra fine $LiCoO_2$ powders with enhanced properties [14]. After the electrode preparation, the polarization behavior and the impedance of lithium cobalt oxide coated nickel oxide electrodes will be studied in a half-cell. The results will be compared with the results obtained for the cobalt microencapsulated nickel electrodes.

Several theoretical models have been derived for the molten carbonate fuel cathode [20-33]. Earlier approaches to modeling the MCFC cathode have relied on empirical equations, which are restricted to the specific cathode material and design parameters for which the equations have been derived. First principles based theoretical models for MCFC cathode can be divided into the thin film model [31] and the agglomerate model [32]. Wilemski assumed that the MCFC cathode could be described as a cylindrical pore covered with a thin film of electrolyte. Gases flowing through the pore dissolve at the surface of the film and diffuse to the surface of pore and react there. While the model gives good agreement with experimental data, it requires knowledge of the pore dia, length and film thickness. Further, the entire description of the electrode is limited and cannot be used for cathode design analysis or two-dimensional simulations. The more common and popular model for describing the MCFC cathode is the agglomerate model proposed by Selman. In this approach, the electrode is assumed to consist of cylindrical agglomerates completely flooded with electrolyte. Gaseous species move through straight cylindrical channels of macropores. Figure 1 presents a schematic of the agglomerate model as applied to the MCFC cathode. As shown in the figure, the macropore is continuous and extends from the current collector to the aluminate matrix. Adjacent to these macropores are microporous agglomerates covered with a film of electrolyte. Both the macropores and micropores remain segregated and the electrochemical reaction proceeds both on the film (exterior to the agglomerate) and also in the micropores (interior of the agglomerate). Yu and Selman do not consider the varying degree of electrolyte fill in the cathode. Using this model, the polarization characteristics of both the cathode and anode have been analyzed. Further, this approach has also been applied to determine the reaction kinetic parameters through impedance analysis. The performance of the MCFC cathode has been analyzed extensively using the agglomerate model by Prins Janson *et al.* [22] Kunz *et al.* [34] used the agglomerate approach but assumed that the reaction proceeded only on the interior surface of the agglomerate but not on the surface of the film. Further, they incorporated the varying electrolyte fill in the cathode by correlating the porosimetry data to the agglomerate dia. Christensen and Livbjerg who considered the agglomerate as a one-dimensional slab instead of a cylinder also used a similar approach. Fontes *et al.* [33] modified Selman's agglomerate model to account for the electrolyte fill and compared these results to that of Kunz *et al.* [34] They accounted for increase in the amount of electrolyte by the uniform growth of the electrolyte film or the decrease of the effective surface area for reaction. They found that a partially drowned agglomerate model with consideration of reaction on the exterior agglomerate surface provided a more realistic description of the cathode as compared to the homogeneous agglomerate model.

The principal deficiency of the agglomerate model, apart from the simplified pore structure assumed, is the lack of measured values for film thickness and agglomerate radius. Both these parameters cannot be estimated appropriately. The agglomerate radius can be estimated from post-test SEM micrographs. But again this radius is not the same along the whole length of the electrode. Further, as discussed by Prins Jansen *et al.* [22] attempts to estimate the thickness of the film vary by two orders of magnitude. Further, using the agglomerate model it is not possible to determine potential/current variations in directions perpendicular to the depth of the electrode. A pseudo-2D model was used by Fontes *et al.* [35] to determine the effect of different design parameters on the performance of the MCFC cathode. In this approach the local reaction rate was solved separately using the agglomerate approach. This was input as a source function in solving for the potential/current variations in two dimensions. This approach does not convey the true physical picture and is still limited due to the de-coupling of the potential from the reaction rate and the use of the agglomerate radius.

The above problems associated with the agglomerate model can be avoided if we take the alternate approach, namely the volume averaging technique used for porous media as done by Prins-Jansen *et al* [21] and De vidts and White [24]. As compared to the agglomerate model where macropores and micropores remain as separate entities, in this approach the pores in the electrode exist in a single continuum. Further, all three phases co-exist within the porous electrode and reaction proceeds everywhere at the solid/melt interface. Using the volume averaging technique, Prins-Jansen *et al.* [21] developed an impedance model for extracting the reaction and transport parameters from experimental data. Model simulations were fitted to experimental data within a certain confidence interval. They found that the diffusion coefficient of O_2 and CO_2 is three orders of magnitude larger than that estimated from the agglomerate model. Other parameters were of the same magnitude as reported by Yu and Selman. [32]

The model developed by Prins-Jansen *et al.* [21] combines both the electrolyte and gas phases into a single entity during volume averaging. The gas and liquid phase mass transport were not considered separately. In this report, we adopt the volume averaging technique as outlined by De vidts and White [24] for three phase reactions in porous electrodes. Using this approach, volume averaged concentrations of both gaseous and liquid phase reactants are obtained separately. The goal of this study was to use the volume averaging technique for studying the polarization characteristics of the MCFC cathode, which has not been done before. The effect of different design parameters on the electrode performance has also been analyzed. The model considers the potential and current variation in both liquid and solid phases. Further concentration variations in the liquid and gaseous phases are considered separately. Using this approach electrolyte filling can be incorporated at ease in addition to eliminating the problems associated with the agglomerate concept. Also different reaction mechanisms can be studied and homogeneity can be assumed safely.

EXECUTIVE SUMMARY

- Lithium Cobalt oxide was coated on Ni cathode by a sol-gel coating.
- Dissolution of nickel into the molten carbonate melt was less in case of lithium cobalt oxide coated nickel cathodes.
- Lithium cobalt oxide coated nickel shows similar polarization characteristics as nickel oxide.
- A three-phase homogeneous model has been developed and the effect of different parameters analyzed.

EXPERIMENTAL

(a) Lithium cobalt oxide coating on sintered nickel electrodes: Lithium cobalt oxide was coated on to the sintered nickel electrodes by a sol-gel method. The gel was prepared by the following procedure. Lithium acetate and cobalt acetate precursors were taken in 1:1 mole ratio and dissolved in de-ionized water. To this, citric acid (4 moles) and ethylene glycol (1 mole) were added (at RT) and the solution was stirred vigorously at 80^o C. The heating and stirring was continued until a viscous gel was obtained. Sintered nickel electrodes were then dipped in the gel and dried at room temperature. The dipping was repeated in order to get a uniform $LiCoO_2$ precursor layer on the nickel electrodes. Finally the electrodes were calcined at 500^o C to decompose all organics and heat treated at 700^o C to get a $LiCoO_2$ layer on to the nickel electrodes. XRD were performed to confirm the $LiCoO_2$ formation and SEM, EDAX were used to see the surface morphology changes after the coating.

(b) PVA assisted sol-gel coating

Lithium nitrate and cobalt nitrate precursors were taken in 1:1 mole ratio and dissolved in de-ionized water. To this, 2 g of an aqueous solution of polyvinyl alcohol (PVA) was added (5 wt %) and stirred at 90^o C until a viscous gel was obtained. Sintered nickel electrodes of $3cm^2$geometrical area were dipped in this gel and dried in an air oven at 70^o C for 5 hrs to remove the water content. Then, the coated electrodes were calcined at 450^o C and sintered at 700^o C to get a $LiCoO_2$ phase on to the porous nickel electrode. The prepared electrodes were finally characterized by SEM, EDAX and XRD.

(c) Preparation of cobalt coated nickel electrodes

Porous cobalt coated nickel cathode was made by a tape casting and sintering process. Cobalt micro-encapsulation on nickel particles was done by a method developed in our laboratory. The tape casting slurry was prepared by ball milling cobalt coated nickel powder (3-5 μm) in water with suitable binder (PVA) and plasticizer (glycerol). The ball milling was done in two steps. At the first step, 50 g of nickel powder were added to 0.50g of dispersant (Disperbyk-112, BYK Chemie) and milled in de-ionized water for 24 h. After the first de-agglomeration step, 8-10 wt % PVA powder was added and milled for 12 h with a defoamer (Airdefoam™ 60, Air Products). After this step, glycerol was added and milled for another 12 h. Finally the slurry was filtered to remove any solid particle and degassed using a

ROTOVAP®evaporator. The slurry then cast using a doctor blade assembly over a glass plate coated with silicone oil. The drying was performed slowly at room temperature for about 48 hours. The cast cobalt coated nickel tape is then stripped off gently from the glass plate and stored. The tape-casting process is shown Figure 2.

Sintering: - Sintering of the cobalt encapsulated nickel green tapes influences the cathode pore structure and thereby affects its electrochemical performance. TGA was done to determine the optimum heat treatment schedule for sintering. A typical TGA curve for green cobalt coated nickel tape is shown in Figure 3. The as cast cobalt coated Ni tape is pre-heated at 120^{o}C for 12 hours in order to remove all the water in the tape. TGA analysis was done by heating the sample from 100^{o}C to 650^{o}C at a rate of 10^{o}C/min. A steep reduction in weight (15 wt%) is seen on heating the sample to 200^{o}C due to the removal of the binder. A secondary weight loss (5 wt%) is noticed between 300^{o}C to 400º C due to the removal of plasticizer. The removal of all volatile and decomposable organic matter is completed below 400^{o}C. On heating the sample above 400º C oxidation of nickel surface takes place. The total weight loss varies between 15 to 20 wt % depending upon the binder and plasticizer contents in the green tapes. Since, Ni is oxidized beyond 400 ºC, it is critical to heat the sample in a reducing atmosphere to prevent oxidation during sintering. Further, the rate of heating should be very slow initially to ensure complete burn out of binder and plasticizer. Based on the above TGA analysis, we chose the following heating pattern to be followed for sintering of the electrodes. Green tapes were cut out to specific area (10 cm x 10 cm) and were placed between two porous alumina plates inside a programmable tube furnace. The heating schedule is shown in Figure 4.

RESULTS AND DISCUSSION

Scanning Electron Micrograph and XRD: - Figure 5 shows the SEM images of Ni and lithium cobalt oxide coated nickel electrodes prepared by the two different methods. The $LiCoO_2$ precursor gel formed thin film on the nickel surface Fig. 5 (b). After sintering at 700^{o}C, the organic matters in the precursor gel decomposed leaving a $LiCoO_2$ coating on the substrate nickel electrode Fig. 5 (c). It was the case in PVA assisted sol-gel coating. The Co content on the nickel electrodes were confirmed by EDAX results Fig. 6. In the conventional sol-gel coating as much as 91 % of cobalt content was observed while PVA assisted sol-gel yielded only 24 % of cobalt on the nickel surface. The formation of the $LiCoO_2$ on the nickel electrode was confirmed by the XRD results Fig. 7. $Li_{0.21}Co_{0.79}O$ was the product formed on the surface of the nickel electrodes during the annealing process. Porosity measurement using liquid absorption technique showed 58 % porosity for the conventional sol-gel coated electrodes and 56.8 % for the PVA assisted sol-gel coated electrodes.

Fig. 8 shows the SEM image of the tape cast cobalt coated nickel electrode. Cobalt encapsulation on the sintered nickel electrode may result in poor porosity and pore size distribution causing poor cell performance. In the case of cobalt coated nickel powder tape casting the state-of-the art porosity and pore size distribution are expected and the SEM results supported this. That is, the average pore size is around 5.7 μm. Nearly 75 % porosity was obtained using the preliminary liquid absorption technique. Detailed pore volume analysis is needed to support the better pore structure of these electrodes. EDAX analysis showed that nearly 7 % of cobalt was deposited on the nickel surface.

Stability tests: -

The $LiCoO_2$ coated electrodes were immersed in molten Li_2CO_3 and K_2CO_3 at 650^o C. Carbonate melt sample was taken at every 10 hours and continued till 200 hours. Then, the carbonate samples were dissolved in 10 % dilute acetic acid. Atomic absorption (AA) was used to analyze the dissolved nickel and cobalt in the melt. Figure 9 shows the results of AA analysis on the amount of dissolved nickel and cobalt in the carbonate melt as a function of time. As shown in the plot, the solubility of Ni^{2+} was more than two times higher in case of bare nickel when compared to that of lithium cobalt oxide coated nickel. Solubility of cobalt was about one order of magnitude lesser than that of nickel. The results indicate that cobalt is more resistive to the molten carbonate environment. The amount of nickel and cobalt cations in the carbonate melt increases with time and saturates after about 100 hours. Similar results have been obtained in the literature for the solubility of Ni^{2+} and Co^{2+} ions in the carbonate melt [36-41]. Based on our data and prior results we can conclude that cobalt coating will decrease the dissolution of nickel in the melt. Both the conventional sol-gel coated and PVA assisted sol-gel coated electrodes showed the same dissolution behavior in molten alkali carbonate melt at 650^o C. The nickel content of both the sol-gel coated nickel electrodes in the melt after 200 hrs of immersion is found to be 17 mole ppm. While cobalt encapsulated nickel electrode showed considerably lesser amount of nickel (12 mole ppm) after 200 hrs of immersion. From the obtained results it can be concluded that the cobalt encapsulation on the sintered nickel electrodes will provide more stability in molten carbonate environment than the sol-gel $LiCoO_2$ coated ones.

Electrochemical Characterization of Cathode: In order to understand further the kinetics of oxygen reduction on $LiCoO_2$ coated NiO, impedance measurements were carried out at different gas compositions. EIS analysis was carried out at equilibrium potential (open circuit) on the NiO and $LiCoO_2$ coated NiO electrodes. Figure 10 shows the impedance analysis of NiO electrode at different temperatures at a particular gas composition. The impedance response is characterized by the presence of high frequency loop and an extension at low frequencies. The high frequency plot has been associated with the charge transfer processes while the low frequency loop to a slow process (mass transfer or slow homogeneous reactions). The impedance response shown in Figure 10 is similar in appearance to the ones obtained by Yuh *et al*. [39, 40] under similar conditions.

Figures 11a and 11b show the impedance response of $LiCoO_2$ coated NiO electrode as a function of different gas composition. The impedance responses appear differently in case of $LiCoO_2$ coated NiO when compared to those of NiO. The two distinct loops occurring at high and low frequencies in the case of NiO appear to be merged with each other in case of $LiCoO_2$ coated NiO. From Figures 11a and 11b, it can also be seen that the effect of partial pressure of O_2 and CO_2 are antagonistic to each other. The magnitude of the impedance loop decreased on increasing the O_2 partial pressure. This clearly indicates a positive reaction order for oxygen and is similar to the response seen for NiO [42]. In case of CO_2, the impedance value increased with an increase in CO_2 partial pressures implying that the reaction order of CO_2 must be negative. Yuh *et al.* [43] obtained similar results for NiO in terms of O_2 and CO_2 dependence on impedance responses.

Development of Theoretical Model

In the molten carbonate fuel cell, oxygen and CO_2 combine at the cathode to form carbonate ions. At the anode hydrogen combines with the carbonate ions from the cathode to form CO_2 and water. The net reaction results in the formation of water with no harmful side reactions. The system of interest to us is the cathode where reduction of oxygen occurs. In order to overcome the difficulties associated with the agglomerate approach, we start by considering a cross-section of the porous electrode as shown in Figure 12. No difference is made between the macropores and micropores while deriving the model equations. The primary reaction in the MCFC cathode is oxygen reduction, which is given by:

$$\tfrac{1}{2}O_2 + CO_2 + 2e^- \rightarrow CO_3^{2-} \tag{1}$$

The above reaction occurs at the interface between the NiO particle and the electrolyte. We neglect any changes in the concentration of the carbonate ions and assume that the concentration of the electrolyte does not change. Further, we assume that the system is at steady state and neglect any changes in cathode due to corrosion. Finally, we neglect changes in temperature in the cathode. Based on these assumptions we next proceed to derive the volume-averaged equations describing transport and reaction in the MCFC cathode.

Concepts and Definitions of Volume Averaging:

In this section, equations are derived for a porous electrode consisting of three phases: solid, liquid and gas. Following De vidts and White we consider a small elemental volume V. This volume should be small compared to the overall dimensions of the porous electrode. But it should be large enough to contain all three phases (see Figure 12). Also it should result in meaningful local average properties. This volume is so chosen that adding pores around this volume does not result in a change in the local average properties. There is no concept of dual porosity where we consider macropores to be filled with the gas and micropores to be occupied by the electrolyte. Rather pores of all sizes are filled with both the electrolyte and the gas, which is more realistic. Some basic definitions of volume averaging have to be presented before understanding the development of the model equations.

Superficial volume average $\overline{\psi}$ and the intrinsic volume average $\langle \psi \rangle$ are defined as

$$\overline{\psi}^{(i)} \equiv \frac{1}{V} \int_{V_{(i)}} \psi \, dV \tag{2}$$

$$\langle \psi \rangle^{(i)} \equiv \frac{1}{V_{(i)}} \int_{V_{(i)}} \psi \, dV \tag{3}$$

Here the superscript *i* represents the phase. The superficial and intrinsic volume averages are related by the porosity.

$$\overline{\psi}^{(i)} = \varepsilon^{(i)} \left\langle \psi \right\rangle^{(i)} \tag{4}$$

Whenever volume averages of the gradients and the divergence appear they should be replaced by the gradients and divergence of the volume averages as below. These are referred to as the theorem of the local volume average of the gradient and the divergence [28, 29]

$$\overline{\nabla \psi}^{(l)} = \nabla \overline{\psi}^{(l)} + \frac{1}{V} \int\limits_{S_{\mathrm{lg}}} \psi^{(l)} n_{(\mathrm{lg})} dS + \frac{1}{V} \int\limits_{S_{\mathrm{l}s}} \psi^{(l)} n_{(\mathrm{l}s)} dS \tag{5}$$

$$\overline{\nabla \cdot \psi}^{(l)} = \nabla \cdot \overline{\psi}^{(l)} + \frac{1}{V} \int\limits_{S_{\mathrm{lg}}} \psi^{(l)} \cdot n_{(\mathrm{lg})} dS + \frac{1}{V} \int\limits_{S_{\mathrm{l}s}} \psi^{(l)} \cdot n_{(\mathrm{l}s)} dS \tag{6}$$

Mass transport equations:

Mass transport occurs in the liquid and gas phases. Both oxygen and carbondioxide gas are fed to the MCFC cathode through the current collector. Both O_2 and CO_2 diffuse through the macropores in the cathode, dissolve in the melt and are transferred by diffusion to the surface of the NiO particles. The material balance in the liquid and gas phases for any species *i* is given by

$$\frac{\partial c_i^{(l)}}{\partial t} + \nabla \cdot N_i^{(l)} = 0 \qquad i = CO_2, O_2 \tag{7}$$

$$\frac{\partial c_i^{(g)}}{\partial t} + \nabla \cdot N_i^{(g)} = 0 \tag{8}$$

There is no bulk reaction. All reactions are assumed to take place at the electrolyte-electrode interface. This is denoted by the normal vector n_{ls} in Fig. 12. Gas diffuses into the electrolyte at the normal interface n_{gl} and reacts at the interface of the electrolyte with the solid catalyst particles, n_{ls}. Hence the homogeneous reaction rate is neglected. Fick's law gives molar flux in the liquid and gas phases.

$$N_i^{(l)} = -D_i^{(l)} \nabla c_i^{(l)} + c_i^{(l)} v^* \tag{9}$$

Binary diffusion is assumed in the gas phase. For a binary system the mass flux relative to the mass average velocity $j_{(A)}$ is given by (9)

$$j_{(A)} = -\frac{c^2}{\rho} M_{(A)} M_{(B)} D_{(AB)} \nabla x_{(A)} \tag{10}$$

where A refers to O_2 and B refers to CO_2.

The relation between $J^{\Diamond}_{(A)}$ (molar flux relative to molar average velocity), $j^{\Diamond}_{(A)}$ (mass flux relative to molar average velocity) and $j_{(A)}$ for a binary system is given by

$$J^{\Diamond}_{(A)} = \frac{j^{\Diamond}_{(A)}}{M_{(A)}} \tag{11}$$

$$j^{\Diamond}_{(A)} = \frac{M}{M_{(B)}} j_{(A)} \tag{12}$$

The relation between $N_{(A)}$ (molar flux with respect to a fixed frame of reference) and $J^{\Diamond}_{(A)}$

$$J^{\Diamond}_{(A)} = N_{(A)} - c_{(A)} v^{\Diamond} \tag{13}$$

When convection is neglected

$$N_{(A)} = J^{\Diamond}_{(A)} \tag{14}$$

Hence

$$N_{(A)} = -cD_{(AB)} \nabla x_{(A)} \tag{15}$$

$$x_{(A)} = \frac{c_{(A)}}{c} \tag{16}$$

$$N_{(A)} = \frac{c_{(A)}}{c} D_{(AB)} \nabla c - D_{(AB)} \nabla c_{(A)} \tag{17}$$

In general for a binary gas the flux is given by,

$$N_i^{(g)} = -D_i^{(g)}\nabla c_i^{(g)} + D_i^{(g)}\left(\frac{c_i^{(g)}}{c^{(g)}}\right)\nabla c^g \tag{18}$$

Using the definitions of volume averaging we obtain the volume averaged flux in both phases as,

$$\overline{N}_i^{(l)} = -D_i^{(l)}\left(\varepsilon^{(l)}\right)^{b-1}\nabla\left(\varepsilon^{(l)}\left\langle c_i\right\rangle^{(l)}\right) \tag{19}$$

$$\overline{N}_i^{(g)} = -D_i^{(g)}\left(\varepsilon^{(g)}\right)^{b-1}\nabla\left(\varepsilon^{(g)}\left\langle c_i\right\rangle^{(g)}\right) + D_i^{(g)}\left(\varepsilon^{(g)}\right)^{b-1}\frac{\left\langle c_i\right\rangle^{(g)}}{\left\langle c\right\rangle^{(g)}}\nabla\left(\varepsilon^{(g)}\left\langle c\right\rangle^{(g)}\right) \tag{20}$$

Volume averaging Eqns. 7 and 8 and substituting the above definitions in Eqns. 19 and 20 gives the following volume averaged mass balance equations,

$$\frac{\partial \overline{c}_i^{(l)}}{\partial t} + \nabla\cdot\overline{N}_i^{(l)} + \overline{F}_i^{(\mathrm{lg})} - \overline{R}_i^{ls} = 0 \tag{21}$$

$$\frac{\partial \overline{c}_i^{(g)}}{\partial t} + \nabla\cdot\overline{N}_i^{(g)} - \overline{F}_i^{(\mathrm{lg})} - \overline{R}_i^{gs} = 0 \tag{22}$$

where $\overline{F}_i^{(\mathrm{lg})}$**,** $\overline{R}_i^{ls}$ and $\overline{R}_i^{gs}$ are all derived from jump balances. $\overline{F}_i^{(\mathrm{lg})}$ is the flux of species *i* from the liquid to the gas phase, $\overline{R}_i^{ls}$ the rate of heterogeneous reaction at the liquid solid interface and $\overline{R}_i^{gs}$ at the gas solid interface.

$$\overline{F}_i^{(\mathrm{lg})} = a^{(\mathrm{lg})} r_i^{(\mathrm{lg})} \tag{23}$$

$$r_i^{(\mathrm{lg})} = k_i^{(\mathrm{lg})}\left(\frac{\left\langle c_i\right\rangle^{(l)}}{K_{e,i}} - \left\langle c_i\right\rangle^{(g)}\right) \tag{24}$$

where for any species *i*, k_i is the mass transfer coefficient and $K_{e,i}$ is the distribution coefficient. Rate of production of species *i* at the solid liquid interface is expressed in terms of the local current density. Butler-Volmer kinetics is assumed for the reaction at the electrode electrolyte interface.

$$\overline{R}_i^{(ls)} = -\sum_k \frac{s_{ik} a^{(sl)}}{n_k F} < j_k >^{(sl)} \tag{25}$$

$$< j_k >^{(sl)} = i_0 \left\{ \left(\frac{< c_{CO_2} >^{(l)}}{< c^*_{CO_2} >^{(l)}} \right)^{-2} \exp(\frac{\alpha_a F \phi}{RT}) - \left(\frac{< c_{CO_2} >^{(l)}}{< c^*_{CO_2} >^{(l)}} \right)^{-1} \left(\frac{< c_{O_2} >^{(l)}}{< c^*_{O_2} >^{(l)}} \right)^{\frac{1}{2}} \exp(-\frac{\alpha_c F \phi}{RT}) \right\}$$

(26)

Here $< j_k >^{(sl)}$ is the local current density at the solid liquid interface and i_0 and i_0^0 are the concentration dependent and concentration independent exchange current densities respectively [26]. The anodic and cathodic reaction orders p_1, p_2 and q_1, q_2 have values of –2, 0, -1, 1/2 respectively.

$$i_0 = i_0^0 \left(\left\langle c_{CO_2} \right\rangle^* \right)^{r_1} \left(\left\langle c_{O_2} \right\rangle^* \right)^{r_2} \tag{27}$$

where r_1 and r_2 have a value of –1.25 and 3.75 respectively for the peroxide mechanism. These values will be different for other mechanisms [22, 26]. At the gas-solid interface there is no reaction. Hence,

$$\overline{R}_i^{(gs)} = 0 \tag{28}$$

Charge transfer equations:

Since we neglect any changes in the concentration of CO_3^{2-}, the effect of migration need not be considered. Hence, Ohms' law is valid in both the solid and liquid phases.

$$i^{(l)} = -\kappa \nabla \phi^{(l)} \tag{29}$$

$$i^{(s)} = -\sigma \nabla \phi^{(s)} \tag{30}$$

Volume averaging the current in the solid and liquid phases results in the following equations.

$$\bar{i}^{(l)} = -\kappa \left(\varepsilon^{(l)} \right)^{d-1} \nabla \left(\varepsilon^{(l)} \left\langle \phi \right\rangle^{(l)} \right) \tag{31}$$

$$\bar{i}^{(s)} = -\sigma \left(\varepsilon^{(s)} \right)^{d-1} \nabla \left(\varepsilon^{(s)} \left\langle \phi \right\rangle^{(s)} \right) \tag{32}$$

The condition of electroneutrality applies everywhere within the electrode. This means that the net sum of the solution and solid phase currents should be constant.

$$\nabla \cdot (\bar{i}^{(l)} + \bar{i}^{(s)}) = 0 \tag{33}$$

Further, any current leaving the solid phase has to enter the liquid phase through the electrochemical reaction. Applying a balance on the solution phase current gives,

$$\nabla \cdot \bar{i}^{(l)} = a^{(sl)} \left\langle j_k \right\rangle^{(sl)} \tag{34}$$

In the above equation the gradient in the solution phase current is proportional to the reaction rate at the solid-liquid interface. Substituting Eq. 34 into Eq. 33 we have,

$$\nabla \cdot \bar{i}^{(s)} = -a^{(sl)} \left\langle j_k \right\rangle^{(sl)} \tag{35}$$

Next, we define the overpotential as $\langle \phi \rangle = \langle \phi \rangle^{(s)} - \langle \phi \rangle^{(l)}$. Combining Eqns. 31 – 35 and using the definition for overpotential results in,

$$\frac{\partial^2 \langle \phi \rangle}{\partial x^2} = a^{(sl)} \left\langle j_k \right\rangle^{(sl)} \left(\frac{1}{\sigma \left(\varepsilon^{(s)} \right)^d} + \frac{1}{\kappa \left(\varepsilon^{(l)} \right)^d} \right) \tag{36}$$

Governing equations:

Combining the above set of equation, assuming steady state, and introducing the dimensionless variables we arrive at the following governing model equations.

$$\frac{\partial}{\partial x^*} \cdot \left[D^{(l)} \left(\varepsilon^{(l)} \right)^{b-1} \frac{\partial}{\partial x^*} \left(\varepsilon^{(l)} \right) u_i^{(l)} \right] - \frac{a^{(\mathrm{lg})} k_i^{(\mathrm{lg})} l^2}{K_{e,i}} \left(u_i^{(l)} - u_i^{(g)} \right) - \frac{s_{ik} a^{(sl)} l^2}{n_k F \left\langle c \right\rangle_i^{(l)*}} < j_k >^{(sl)} = 0$$

(37)

$$D_i^{(g)}\frac{\partial}{\partial x^*}\cdot\left[\left(\varepsilon^{(g)}\right)^{b-1}\frac{\partial}{\partial x^*}\left(\varepsilon^{(g)}u_i^{(g)}\right)\right]$$

$$-D_i^{(g)}\frac{\partial}{\partial x^*}\cdot\left[\left(\varepsilon^{(g)}\right)^{b-1}\frac{u_i^{(g)}}{\langle c\rangle_{CO_2}^{(g)*}u_{CO_2}^{(g)}+\langle c\rangle_{O_2}^{(g)*}u_{O_2}^{(g)}}\frac{\partial}{\partial x^*}\left(\varepsilon^{(g)}\left(\langle c\rangle_{CO_2}^{(g)*}u_{CO_2}^{(g)}+\langle c\rangle_{O_2}^{(g)*}u_{O_2}^{(g)}\right)\right)\right]$$

$$+a^{(\mathrm{lg})}k_i^{(\mathrm{lg})}\left(u_i^{(l)}-u_i^{(g)}\right)=0 \tag{38}$$

$$\frac{\partial^2 F\langle\phi\rangle/RT}{\partial x^{*2}}=a^{(sl)}l^2\langle j_k\rangle^{(sl)}\left(\frac{1}{\sigma\left(\varepsilon^{(s)}\right)^d}+\frac{1}{\kappa\left(\varepsilon^{(l)}\right)^d}\right)\frac{F}{RT} \tag{39}$$

The following dimensionless variables have been used in arriving at these equations.

$$u_i^{(l)}=\frac{\langle c\rangle_i^{(l)}}{\langle c\rangle_i^{(l)*}},u_i^{(g)}=\frac{\langle c\rangle_i^{(g)}}{\langle c\rangle_i^{(g)*}}$$

Since we consider the transport of O_2 and CO_2 in the liquid and solid phases, we have five governing equations - four transport equations (Eq. 37 and 38) and one equation for the polarization (Eq. 39). We assume the problem is one-dimensional and neglect any changes in planes perpendicular to the *x* axis.

Boundary conditions:

Since, the gases are fed at the current collector side of the cathode, in the gas phase the concentrations are equal to the inlet concentration. In the solution phase, the concentrations are given by Henry's law. At the separator side (matrix) the flux of all species is equal to zero. Also all the current is carried by the ions at the separator end and by electrons at the current collector end. Based on these conditions the boundary condition at the current collector is given by,

$$\langle c_i\rangle^{(l)}=\langle c_i\rangle^{(l)*},\langle c_i\rangle^{(g)}=\langle c_i\rangle^{(g)*},\frac{\partial\langle\varphi\rangle}{\partial x}=-\frac{\mathrm{I_{tot}}}{\sigma\left(\varepsilon^{(s)}\right)^d}\qquad \text{at}\quad x=0 \tag{40}$$

At the matrix (x=L),

$$\frac{\partial\left\langle c_i\right\rangle^{(l)}}{\partial x}=0,\frac{\partial}{\partial x}\left(\frac{\partial}{\partial x}\left(\varepsilon^{(g)}\left\langle c_i\right\rangle^{(g)}\right)+\left\langle\frac{c_i^{(g)}}{c^{(g)}}\right\rangle\frac{\partial}{\partial x}\left(\varepsilon^{(g)}\left\langle c\right\rangle^{(g)}\right)\right)=0,\frac{\partial\left\langle\varphi\right\rangle}{\partial x}=\frac{\mathrm{I}_{\mathrm{tot}}}{\kappa\left(\varepsilon^{(l)}\right)^d} \tag{41}$$

Expressing them in terms of the dimensionless variables

$$u_i^{(l)}=1,u_i^{(g)}=1,\frac{\partial F\left\langle\varphi\right\rangle/RT}{\partial x^*}=-\frac{\mathrm{I}_{\mathrm{tot}}L}{\sigma\left(\varepsilon^{(s)}\right)^d}\frac{F}{RT}\qquad \text{at}\quad x^*=0 \tag{42}$$

$$\frac{\partial u_i^{(l)}}{\partial x^*}=0,\frac{\partial}{\partial x^*}\left(\frac{\partial}{\partial x^*}\left(\varepsilon^{(g)}u_i^{(g)}\right)+\left\langle\frac{u_i^{(g)}}{\left\langle c\right\rangle_{CO_2}^{(g)*}u_{CO_2}^{(g)}+\left\langle c\right\rangle_{O_2}^{(g)*}u_{O_2}^{(g)}}\right\rangle\frac{\partial}{\partial x^*}\left(\varepsilon^{(g)}\left\langle c\right\rangle^{(g)}\right)\right)=0,$$
$$\frac{\partial F\left\langle\varphi\right\rangle/RT}{\partial x}=\frac{\mathrm{I}_{\mathrm{tot}}}{\kappa\left(\varepsilon^{(l)}\right)^d}\qquad \text{at}\quad x^*=1 \tag{43}$$

Based on these equations the following dimensionless groups can be written

$$\delta=a^{(sl)}l^2 i_0\left(\frac{1}{\sigma\left(\varepsilon^{(s)}\right)^d}+\frac{1}{\kappa\left(\varepsilon^{(l)}\right)^d}\right)\frac{F}{RT} \tag{44}$$

$$\gamma_1=\frac{\mathrm{I}_{\mathrm{tot}}l}{\sigma\left(\varepsilon^{(l)}\right)^d}\frac{F}{RT} \tag{45}$$

$$\gamma_2=\frac{\mathrm{I}_{\mathrm{tot}}l}{\kappa\left(\varepsilon^{(s)}\right)^d}\frac{F}{RT} \tag{46}$$

List of Parameters

The parameters used in the model are given in Table I. Gas phase diffusion coefficients were estimated using the Fuller correlation [30]. It can also be estimated using the Chapman-Enskong equation. According to the Fuller correlation

$$D=\frac{10^{-3}T^{1.75}\left(1/\widetilde{M}_{CO_2}+1/\widetilde{M}_{O_2}\right)^{1/2}}{p\left[\left(V_{CO_2}\right)^{1/3}+\left(V_{O_2}\right)^{1/3}\right]^2} \tag{47}$$

The diffusion volumes have been listed by Cussler [30] as $V_{CO_2} = 26.9$ and $V_{O_2} = 16.6$. At 923 K and 1 atm the binary diffusion coefficient has been estimated as 1.16 cm^2/s.

IR-free polarization

The model equations are highly nonlinear and coupled in nature and hence cannot be solved analytically. The five governing equations (Eq. 37-39) with the appropriate boundary conditions (Eq. 40 and 41) have been solved simultaneously using Femlab 2.1 and also using Band. In studying the performance of the cathode, the main parameter of interest is the electrode polarization under different applied currents. The measured polarization is the difference in potential between the current collector $(\Phi_M)_o$ under load as compared to at open circuit $(\Phi_M)_{o,OCV}$. However, the model solves for the local overpotential ϕ, which is the difference between the solid phase and liquid phase potential. Lee *et al.* [20] present a relationship between this overpotential and the experimentally measured polarization loss (Φ_{Mo}-$\Phi_{Mo,OCV}$). The IR free polarization is given as,

$$\phi_{IR-free} = (\Phi)_0 + \frac{1}{1+\kappa_{app}/\sigma_{app}}\left[(\Phi)_L - (\Phi)_0\right]$$

where κ_{app} and σ_{app} are the apparent conductivities modified by the porosity
Next, we discuss the effect of different parameters on the IR free polarization loss.

Effect of Conductivity:

Ohmic losses in the MCFC cathode can arise due to poor conductivity of either the electrode or the electrolyte. The electrolyte here is an eutectic mixture of Li_2CO_3-K_2CO_3 held in a lithium aluminate matrix. Electrolyte fills inside the porous cathode due to capillary forces. In general the conductivity of the electrode material is much larger than that of the electrolyte. The conductivity of the melt lies in the order of 10^{-2} S/cm while solid phase (electrode) conductivities lie in the order of 10 S/cm. Figure 13 presents the polarization loss at various loads for different values of the electrolyte conductivity. The model simulations were run with a σ value of 13 S/cm. From Fig. 13 it can be seen that increase in κ decreases the polarization loss. At large values of κ (1.5 S/cm) a linear relationship is seen between the polarization loss and the applied load. With decreasing values of κ, the polarization loss increases exponentially with increasing applied current. For κ=1.5X10^{-2} S/cm it can be seen that changing the applied current from 80 mA/cm^2 to 160 mA/cm^2 results in increasing the polarization loss more than 3 times. A similar change in current for κ=1.5 S/cm would increase the polarization loss only 1.5 times. While the model simulations show a significant effect of the electrolyte conductivity on electrode performance, in reality the choice of electrolyte is limited by other considerations. Stability at high temperatures, low dissolution of cathode material and current collector in the melt and cost play a critical role in limiting the choice to a few eutectic mixtures. While the difference in conductivity between these different melts is not significant, the effective electrolyte conductivity depends strongly on the cathode design. The effective electrolyte conductivity is affected by the degree of electrolyte fill in the cathode, which in turn is influenced by the number of macropores and micropores in the cathode. In order to study this we plot the local overpotential across the thickness of the electrode for different κ values. As seen from Figure 14, the difference between the solid and liquid phase potentials increases with increase in distance from the current collector. With decreasing values of κ most of the polarization drop occurs close to the matrix.

Figure 15 and 16 present the change in reaction rate di_2/dx across the thickness of the electrode. The reaction rate is plotted as a function of two different parameters. The dimensionless parameter γ_2 is a measure of the electrolytic conductivity in the porous electrode. As seen from Fig. 15 changes in this parameter have a significant effect on the reaction rate di_2/dx. These simulations have been done after fixing the ohmic conductivity of the electrode, i.e. γ_1. With increase in γ_2 (low electrolytic conductivity), the reaction rate increases at the end of the electrode. In general it can be seen that poor electrolytic conductivity as compared to ohmic conductivity leads to very poor reaction rate distribution across the electrode. In general it is preferable to have an electrode with a uniform reaction rate distribution everywhere within the electrode. The model simulations indicate that if γ_1 and γ_2 differ significantly (over 2 orders of magnitude) most of reaction occurs within a zone close to the electrolyte matrix. The rest of the electrode does not take part in the reaction and represents a loss of effective active material. Figure 16 presents the model results when both γ_1 and γ_2 are comparable to each other. In this case it can be clearly seen that the reaction rate is uniformly distributed across the electrode. When the electrolytic and ohmic conductivities are equal to each other a symmetrical reaction rate distribution curve is obtained. Although this is the desirable scenario practical considerations limit us from achieving this. As mentioned before, in general solid phase conductivities are much larger than liquid phase conductivities. Hence, the actual electrode utilization is not 100% but much lower than that. Using this theoretical model it is possible to optimize the electrode thickness based on input electrode parameters.

Effect of Exchange Current Density:

We next study the effect of reaction kinetics on the electrode performance. Various mechanisms have been proposed for the cathode reaction in MCFC. While the exact nature of the reaction is under discussion, the rate of the reaction can be measured easily. Similar to electrolyte conductivity, the oxygen reduction rate does not vary significantly on different materials. The state-of-art cathode material in MCFC is NiO with an i_o of 0.81 mA/cm^2. Alternate materials such as $LiCoO_2$ (i_o=0.15 mA/cm^2) and $LiFeO_2$ (i_o=0.1 mA/cm^2) have been tested as cathodes since they exhibit lower corrosion rates in the melt. Figure 17 presents the polarization loss at different currents for various i_o values. As seen from the plot, varying i_o has a significant effect on the polarization loss. As i_0 decreases the overpotential increases as result of increased kinetic resistance as shown in Fig.16. Similar to κ at low values of i_o the polarization loss increases linearly with increasing applied loads. However, at low values of i_o the polarization loss increases asymptotically and reaches a plateau with increase in current. This is in contrast to Fig. 14 where decrease in kappa increases the potential drop exponentially.

This is because as i_0 decreases, the concentration drops slowly due to slower reaction kinetics. These results agree well with those reported earlier by Selman. Fontes et al also predicted this. According to them the downward bending effect of the reaction rate and the downward bending effect of the mass transfer rate can be combined to give psuedo-linear polarization curves. Fig. 18 shows that the overpotential increases sharply towards the separator side of the electrode. The simulations were performed for an applied current of 160 mA/cm^2. It can also be seen that a large potential drop close to the electrolyte matrix was observed for low values of i_o. This directly translates to a large polarization drop across the electrode (see Fig. 17).

Effect of diffusion coefficient:

The upward bending effect of the mass transfer resistance is also seen by decreasing the diffusion coefficients in the liquid phase as shown in Fig. 19 and Fig. 20. The overpotential is almost uniform for large diffusion coefficients whereas for small diffusion coefficients the overpotential increases drastically very near the separator region. A similar effect is seen for both O_2 and CO_2. However, the results show that changing the diffusion coefficient by one order of magnitude results in an increase in overpotential of only 50-70 mV. This effect is smaller than that seen for electrolyte conductivity. Currently impedance analysis is being done to determine the diffusion coefficient in the liquid phase. Figure 21 presents a comparison of the liquid phase carbon dioxide concentration across the electrode for different values of the diffusion coefficient. It can be seen that change in diffusion significantly alters the concentration. At very low values of $D_{CO2,l}$ the CO_2 concentration close to the matrix drops to zero. However, the diffusion coefficient in MCFC cathode lies in the order of 10^{-3} cm^2/s. From Fig. 21 it can be seen that this does not deplete the CO_2 all throughout the electrode. However, it can be clearly that a concentration gradient exists across the thickness of the electrode. Similar results are seen for oxygen also.

Effect of gas compositions:

The exchange current density is concentration dependent as discussed earlier. CO_2 concentration is raised to negative power of -1.25 and O_2 concentration is raised to a positive power of 3.35. Increasing the concentration of CO_2 decreases the local current density and hence increases the polarization as shown in Fig 22. The effect is the reverse for O_2 as shown in Fig.23. Prins-Jansen et al have performed impedance analysis and have concluded that the resistance increases with CO_2 concentration and decreases with increasing O_2 concentration, which agrees with the results obtained in this performance model.

Effect of thickness of the electrode:

The resistance to mass transfer increases as the electrode thickness increases. Hence the polarization increases with the thickness as shown in Fig. 24. This agrees with the prediction by Prins-Jansen. Their simulations considered changing the thickness keeping all other parameters constant similar to what has been done here. Yuh obtained an optimum for the dependence on thickness. But he considered a varying electrolyte filling degree with varying thickness. As suggested by Prins-Jansen et al increasing the thickness has two conflicting effects, both the ionic resistance and the active surface area being increased. The upward bending effect with increasing thickness is due to increase in mass transfer resistance. Figure 25 plots the CO_2 gas phase concentration across the electrode thickness. Previous investigators have neglected to consider the effect of changes in gas phase concentration while modeling the MCFC cathode. As seen from Fig. 25, while the concentration does not change significantly, parameters like the electrode thickness do have an effect on the concentration. Since, the liquid phase concentration, and hence the reaction rate and polarization loss, is dependent on the local gas phase concentration any changes in this value are bound to have an effect on the electrode performance. Hence our model simulations indicate that the changes in CO_2 and O_2 gas phase concentration while small cannot be completely neglected.

Finally we compare the model simulations to an experimental polarization curve of NiO. The polarization curve is given in Fig. 26. The curve has been generated with the parameters given in Table I and an applied load of 160 mA/cm^2. NiO is a p type semiconductor and has a lower conductivity than pure Ni. Li^+ ions coming from the electrolyte, diffuse into the NiO and increase its electronic conductivity. However, NiO has much larger exchange current density for oxygen reduction as compared to alternate cathode materials such as CoO_2. Model simulations indicate that an electrode made of a material, which has the conductivity of NiO, and exchange current density of $LiCoO_2$ would suffer around 50% more polarization than the conventional NiO cathode. The cathode polarization results shown in Figure 26 agree with the previous theoretical and experimental investigations of Lee *et al* [20] and hence confirm the validity of the model.

CONCLUSIONS

$LiCoO_2$ coating was successful in reducing the nickel solubility in the carbonate melts. It was evident from the results of solubility of Co encapsulated nickel and of $LiCoO_2$ coated nickel electrodes that the later is inferior in solving the purpose. Also, impedance studies of $LiCoO_2$ coated electrodes showed higher resistance than that of Co microencapsulated ones.

Significant results obtained from the model are summarized below:

- The electrolyte conductivity and exchange current density have very large effect on the performance of MCFC cathode as compared to other parameters. Due to low electrolyte conductivity as compared to solid phase conductivity, most of the polarization loss occurs in a region close to the electrolyte matrix. Most of the material within the center of the electrode does not take part in the electrochemical reaction. This leads to low active material utilization within the electrode. Both low electrode and electrolytic conductivity lead to very poor reaction rate distribution across the electrode.
- Increase in reaction rate as exemplified by the exchange current density leads to decrease in polarization losses. Further, with increase in i_o the polarization loss increases linearly with increasing applied loads. However, at low values of i_o the polarization loss increases asymptotically and reaches a plateau with increase in current.
- The upward bending effect of the mass transfer resistance is seen by decreasing the diffusion coefficients in the liquid phase
- Increasing the concentration of CO_2 decreases the local current density and hence increases the polarization. The effect is the reverse for O_2
- The resistance to mass transfer increases as the electrode thickness increases. Hence the polarization increases with the thickness keeping the electrolyte filling the same for varying thickness.

REFERENCES

[1] A. J. Appleby and F. R. Foulkes, Fuel Cells – Hand Book, Von Nostrand Reinhold, NewYork (1989).

[2] K. Joon, J. Power Sources, **71** (1998) 12.

[3] J. R. Selman, Assesment of research needs for advanced fuel cells by the DOE advanced fuel cell working group (AFCWG), S.S. Penner, Editor, Permagon Press, New York (1984).

[4] T. G. Benamin, E. L. Camara and L. G. Marianowski, Handbook of Fuel Cell Performance, Contract no. EC-77C-03-1545, Chicago, IL, (1980).

[5] L. Christner, L. Paetsch, P.Patel and M. Farooque, Scale-up of internal reforming molten carbonate fuel cells. Proceedings of the 1988 Fuel Cell Seminar, Long Beach, CA (1988) 403.

[6] K. Tanimoto, Y. Miyazaki, M. Yanagida, S. Tanase, T. Kojima, N. Ohtori, H. Okuyama, T. Kodama, Denki Kagaku, **59**(7) (1991) 619.

[7] K. Tanimoto, Y. Miyazaki, M. Yanagida, T. Kojima, N. Ohtori, T. Kodama, Denki Kagaku, **63**(4) (1995) 316.

[8] L. Plomp, E.F. Sitters, C. Vessies, F. C. Eckes, J. Electrochem. Soc., **138**(2) (1991) 629.

[9] L. Giorgi, M. Carewska, S. Scaccia, E. Simonetti, F. Zarzana, Denki Kagaku, **64**(6) (1996) 482.

[10] C. Lagergren, A. Lundblad, B. Bergman, J. Electrochem. Soc., **141**(11) (1994) 2959.

[11] T. Fukui, S. Ohara, H. Okawa, T. Hotta, M. Naito, J. Power Sources, **86** (2000) 340.

[12] X. Zhang, H. Okawa, T. Fukui, Denki Kagaku, **66**(11) (1998) 1141.

[13] S. T. Kuk, Y. S. Song, S. Suh, J. Y. Kim, K. Kim *J. Mat. Chem*, **11**, (2001), 630-635

[14] S.W. Nam, S.G. Kim, I.H. Oh, T.H. Lim, H.Y. Ha, S.A. Hong, K. Kim and H.C. Lim, Carbonate Fuel Cell Technology, *Proceedings of the fifth International Symposium*, pv 99-20, 253-262.

[15] X. Zhang, H. Okawa and T. Fukui, *Electrochemistry*, 66, No. 11, 1998, 1141-1143.

[16] T. Fukui, S. Ohara, H. Okawa, T. Hotta, M. Naito, *J. Power Sources*, 86, (2000), 340-346.

[17] Fang. B, Zhou. C, Liu. X, Duan. S. *J. Appl. Electrochem*. (2001), 31(2), 201-205

[18] New Mohamedi, M.; Hisamitsu, Y.; Kihara, K.; Kudo, T.; Itoh, T.; Uchida, Isamu. *J. Alloys* Compd. (2001), 315 (1-2), 224-233.

[19] New Lada, W.; Deptula, A.; Sartowska, B.; Olczak, T.; Chmielewski, A. G.; Carewska, M.; Scaccia, S.; Simonetti, E.; Giorgi, L.; Moreno, A. Mater. Res. Soc. Symp. Proc. (2000), 623 (Materials Science of Novel Oxide-Based Electronics) 395-400.

[20] G. L. Lee, J. R. Selman and L. Pomp, *J. Electrochem. Soc.*, **140**, 390 (1993).

[21] J. A. Prins-Jansen, J. D. Fehribach, K. Hemmes and J. H. W. de Wit, *J. Electrochem. Soc.*, **143**, 1617 (1996).

[22] J. A. Prins-Jansen, K. Hemmes and J. H. W de Wit, *Electrochem. Acta*, **40**, 3585 (1997).

[23] E. Fontes, C. Lagergren, D. Simonsson, *J. Electroanal. Chem.*, **432**, 121 (1997).

[24] P. de Vidts and R. E. White, *J. Electrochem. Soc.*, **144**, 1343 (1997).

[25] P. de Vidts, “Mathematical modeling of a nickel/hydrogen cell”, Ph.D. Thesis, Texas A & M University, Texas, (1995).

[26] J. Prins-Jansen, “Cathodes in Molten Carbonate Fuel Cells”, Ph.D. Thesis, Netherlands, (1996).

[27] C. Y. Yuh, “Potential Relaxation and AC Impedance of Porous Electrodes”, Ph.D. Thesis, Chicago, Illinois, (1985).

[28] J. C. Slattery, Advanced Transport Phenomena, New York, (1999).

[29] M. Kaviany, Principles of Heat Transfer in Porous Media, New York, (1991).

[30] E. L. Cussler, Diffusion, Mass Transfer in Fluid Systems, New York, (1984).

[31] G. Wilemski, *J. Electrochem. Soc.*, **130**, 117 (1983).

[32] C. Y. Yuh and J. R. Selman, *J. Electrochem. Soc.*, **131**, 2062 (1984).

[33] E. Fontes, C. Lagergren and D. Simonsson, *Electrochem. Acta*, **38**, 2669 (1993).

[34] H. R. Kunz and L. A. Murphy, *J. Electrochem. Soc.*, **135**, 1124 (1988).

[35] E. Fontes, M. Fontes and D. Simonsson, *Electrochem. Acta*, **141**, 1 (1996).

[36] Lange F, Martin M, Beriche Der Bunsen-Gesellschaft –Physical Chemistry Chemical Physics, **101** (2) (1997) 176.

[37] K. Tanimoto, Y. Miyazaki, M. Yanagida, S. Tanase, T. Kojima, N. Ohtori, H. Okuyama, T. Kodama, Denki Kagaku, **59**(7) (1991) 619.

[38] K. Ota, S. Mitsushima, S. Katao, S. Asano, H. Yoshitake, and N. Kamiya, J. Electrochem. Soc., **139**(3) (1992) 667.

[39] X. Zhang, P. Capobianco, A. Torazza, and B. Passalacqua, *Electrochemistry*, **67**(6) (1999).

[40] J. B. J. Veldhuis, F. C. Eckes, and L. Plomp, J. Electrochem. Soc., **139** (1) (1992) L6.

[41] K. Ota, Y. Takeishi, S. Shibata, H. Yoshitake, and N. Kamiya, J. Electrochem. Soc., **142**(10) (1995) 3322.

[42] C. Y. Yuh and J. R. Selman, J. Electrochem. Soc., **138**(12), (1991) 3649.

[43] C. Y. Yuh and J. R. Selman, J. Electrochem. Soc., **138**(12), (1991) 3642.

LIST OF SYMBOLS

$\langle CO_2 \rangle^{g}$	Volume averaged concentration of CO_2 in the gas phase, mol/cm^3
$\langle O_2 \rangle^{g}$	Volume averaged concentration of O_2 in the gas phase, mol/cm^3
$\langle CO_2 \rangle^{l}$	Volume averaged concentration of CO_2 in the liquid phase, mol/cm^3
$\langle O_2 \rangle^{l}$	Volume averaged concentration of O_2 in the liquid phase, mol/cm^3
$\langle CO_2 \rangle^{(g)*}$	Bulk concentration of CO2 in the gas phase, mol/cm^3
$\langle O_2 \rangle^{(g)*}$	Bulk concentration of O2 in the gas phase, mol/cm^3
$\langle CO_2 \rangle^{(l)*}$	Bulk concentration of CO2 in the liquid phase, mol/cm^3
$\langle O_2 \rangle^{(l)*}$	Bulk concentration of O2 in the liquid phase, mol/cm^3
$a^{(lg)}$	Specific surface area at the gas/liquid interface, cm^2/cm^3
$a^{(sl)}$	Specific surface area at the liquid/solid interface, cm^2/cm^3
b	Correction for diffusion coefficeint
c	Total concentration, mol/cm^3
$c_{(i)}$	Concentration of species i, mol/cm^3
d	Correction for conductivity
$D^{(g)}_{CO_2}$	Diffusion coefficient of CO_2 in the gas phase, cm^2/s
$D^{(g)}_{O_2}$	Diffusion coefficient of O_2 in the gas phase, cm^2/s
$D^{(l)}_{CO_2}$	Diffusion coefficient of CO_2 in the liquid phase, cm^2/s
$D^{(l)}_{O_2}$	Diffusion coefficient of O_2 in the liquid phase, cm^2/s
I	Applied current, A/cm^2
i_0^0	Concentration independent exchange current density, A/cm2
i_0	Concentration dependent exchange current density, A/cm2
$i^{(l)}$	Current density in the electrolyte, A/cm^2
$i^{(s)}$	Current density in the solid, A/cm^2
$J^{\Diamond}_{(i)}$	Molar flux of species i relative to molar average velocity, mol/cm^{2}s

$j^{\Diamond}_{(i)}$	Mass flux of species i relative to molar average velocity, mol/cm^{2}s
$j_{(i)}$	Mass flux of species i relative to mass average velocity, mol/cm^{2}s
$\langle j_k \rangle$	Average local current density due to reaction k taking place at the liquid/solid interface, A/cm^2
K_{e,CO_2}	Equilibrium constant relating the concentration of CO_2 in the liquid and gas phase, $\frac{\langle c^*_{CO_2} \rangle^{(l)}}{\langle c^*_{CO_2} \rangle^{(g)}}$
K_{e,O_2}	Equilibrium constant relating the concentration of O_2 in the liquid and gas phase, $\frac{\langle c^*_{O_2} \rangle^{(l)}}{\langle c^*_{O_2} \rangle^{(g)}}$
$k^{(\mathrm{lg})}_{CO_2}$	Rate constant of molar flux of CO_2 between the liquid and gas phase cm/s
$k^{(\mathrm{lg})}_{O_2}$	Rate constant of molar flux of O_2 between the liquid and gas phase cm/s
L	Thickness of the electrode, cm
$M_{(i)}$	Molecular weight of species i, gm/mol
N_i	Molar flux of species i with respect to a fixed frame of reference, mol/cm^{2}s
$\overline{N}^{\mathrm{g}}_{\mathrm{i}}$	Volume averaged molar flux of species i in the gas phase, mol/cm^{2}s
$\overline{N}^{\mathrm{l}}_{\mathrm{i}}$	Volume averaged molar flux of species i in the liquid phase, mol/cm^{2}s
$n_{(\mathrm{lg})}$	Unit normal vector to the surface $S_{(\mathrm{lg})}$ pointing out of the liquid into the gas phase
$n_{(1s)}$	Unit normal vector to the surface $S_{(\mathrm{ls})}$ pointing out of the liquid into the gas phase
$p^*_{CO_2}$	Equilibrium partial pressure of CO_2, atm.
$p^*_{O_2}$	Equilibrium partial pressure of O_2, atm.
$S_{(\mathrm{lg})}$	Surface that coincides with the liquid/gas interface inside volume V, cm^2
$S_{(1s)}$	Surface that coincides with the liquid/solid interface inside volume V, cm^2
V	Volume of porous media, cm^3
$V_{(i)}$	Volume of phase i in the porous media, cm^3

$x_{(i)}$	Mole fraction of species i
$\langle\phi\rangle$	Overpotential, V
$\langle\phi\rangle^{(\mathrm{l})}$	Liquid phase potential, V
$\langle\phi\rangle^{(\mathrm{s})}$	Solid phase potential, V
α_{c}	Cathodic transfer coefficient
α_{a}	Anodic transfer coefficient
$\varepsilon^{(\mathrm{g})}$	Gas porosity
$\varepsilon^{(\mathrm{l})}$	Liquid porosity
$\varepsilon^{(\mathrm{s})}$	Solid porosity
κ	Electrolyte conductivity, S/cm
$\rho_{(i)}$	Density of species i, $\mathrm{gm/cm}^3$
σ	Electrode conductivity, S/cm
v	Mass average velocity, cm/s
$v^{\Diamond}$	Molar average velocity, cm/s

Table I. List of Parameters used in model simulation

Parameter	Value	Reference
Diffusion coefficient of CO2 in the liquid phase, $D_{CO_2}^{(l)}$	1e^{-3} cm^2/s	[21]
Diffusion coefficient of CO2 in the liquid phase, $D_{O_2}^{(l)}$	3e^{-3} cm^2/s	[21]
Diffusion coefficient of CO2 in the gas phase, $D_{CO_2}^{(g)}$	1.16 cm^2/s	[30]
Diffusion coefficient of O2 in the gas phase, $D_{O_2}^{(g)}$	1.16 cm^2/s	[30]
Electrode conductivity, σ	13 S/cm	[20]
Electrode conductivity, κ	1.5e^{-2} S/cm	[21]
Correction for diffusion coefficient, b	1.5	[25]
Correction for conductivity, d	1.5	[25]
Specific surface area at the liquid/solid interface, $a^{(sl)}$	8000 cm^2/cm^3	[27]
Specific surface area at the liquid/gas interface, $a^{(lg)}$	1e^4 cm^2/cm^3	[25]
Equilibrium constant relating the concentration of CO2 in the liquid and gas phase, K_{e,CO_2}	0.01	
Equilibrium constant relating the concentration of O2 in the liquid and gas phase, K_{e,O_2}	0.01	
Rate constant of the molar flux of CO2 between the liquid and gas phase, $k_{CO_2}^{(\lg)}$	3e^{-3} cm/s	[25]
Rate constant of the molar flux of O2 between the liquid and gas phase, $k_{O_2}^{(\lg)}$	2e^{-3} cm/s	[25]
Thickness of the electrode, L	0.09 cm	Measured
Liquid porosity, $\varepsilon^{(l)}$	0.3	Measured
Gas porosity, $\varepsilon^{(g)}$	0.4	Measured
Solid porosity, $\varepsilon^{(s)}$	0.3	Measured
Exchange current density, i_0^0	50 mA/cm^2	[27]
Cathodic transfer coefficient, α_c	0.5	[22, 26]

Cathodic transfer coefficient, α_a	1.5	[22, 26]
r_1	-1.25	[22, 26]
r_2	0.375	[22, 26]

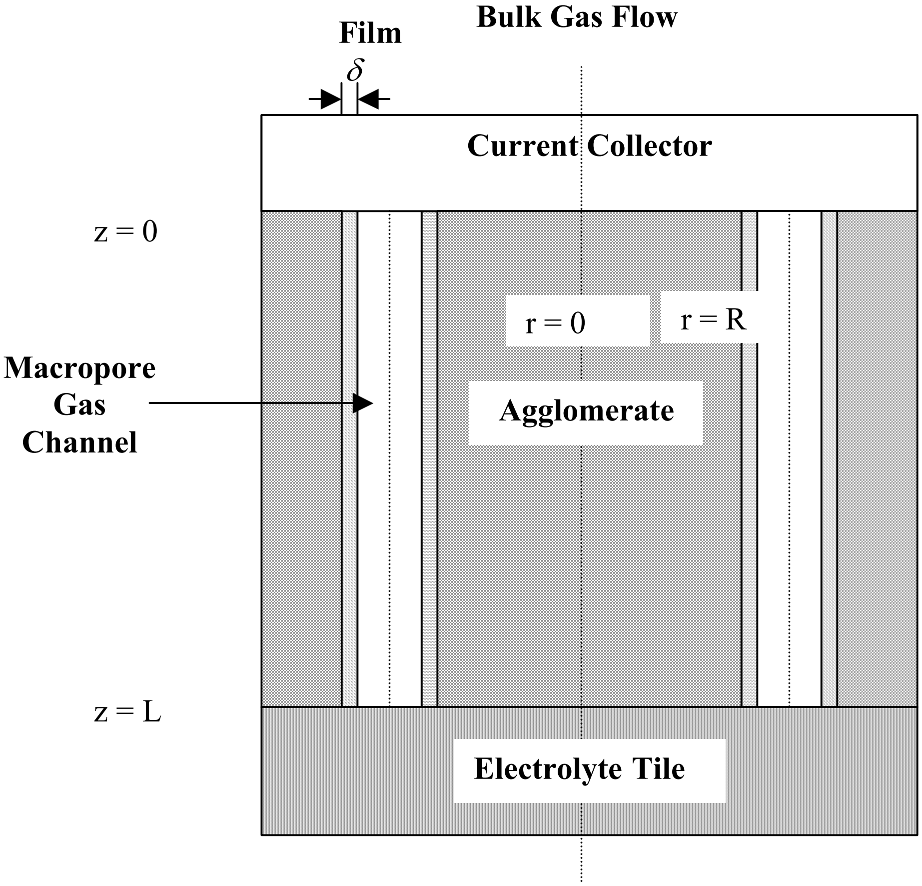

Figure 1. Schematic of the MCFC cell

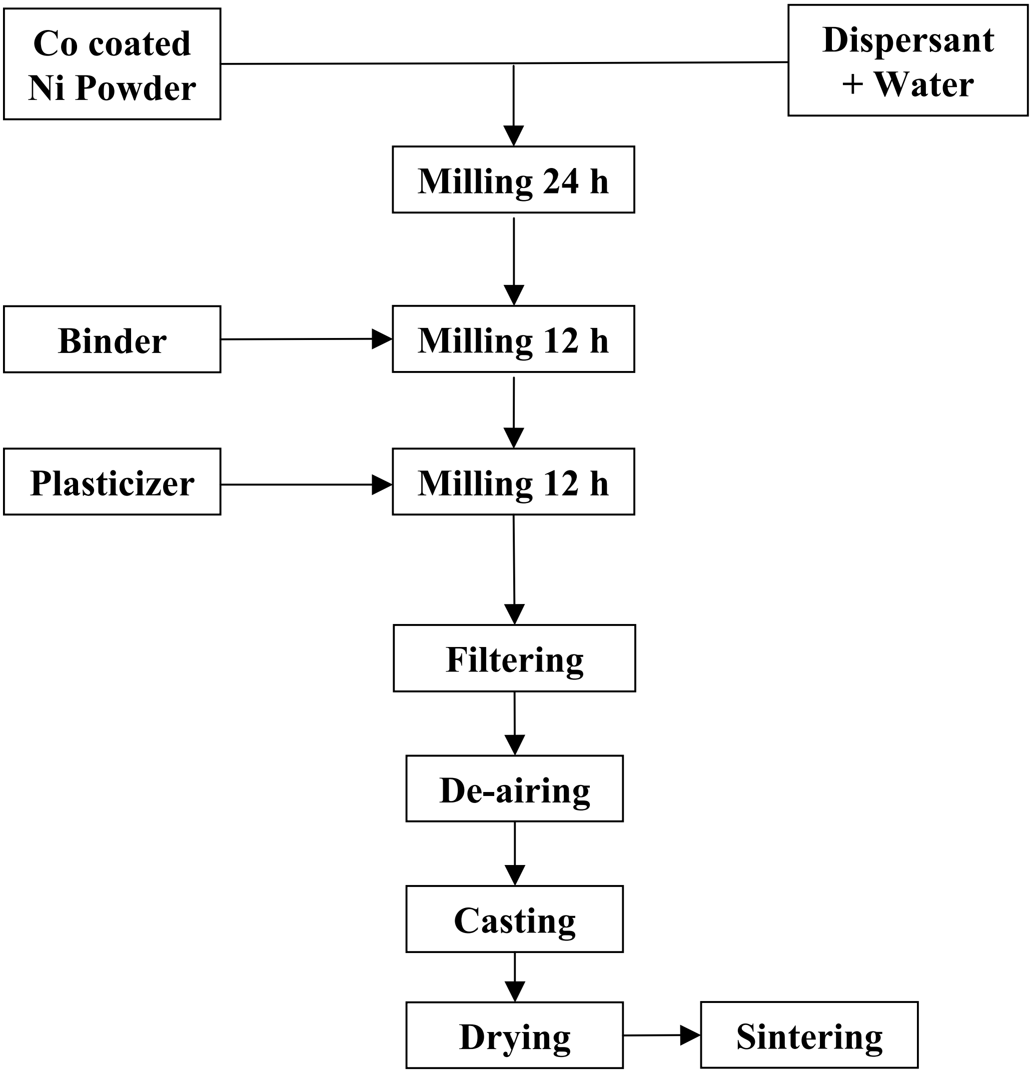

Figure 2. The tape-casting procedure

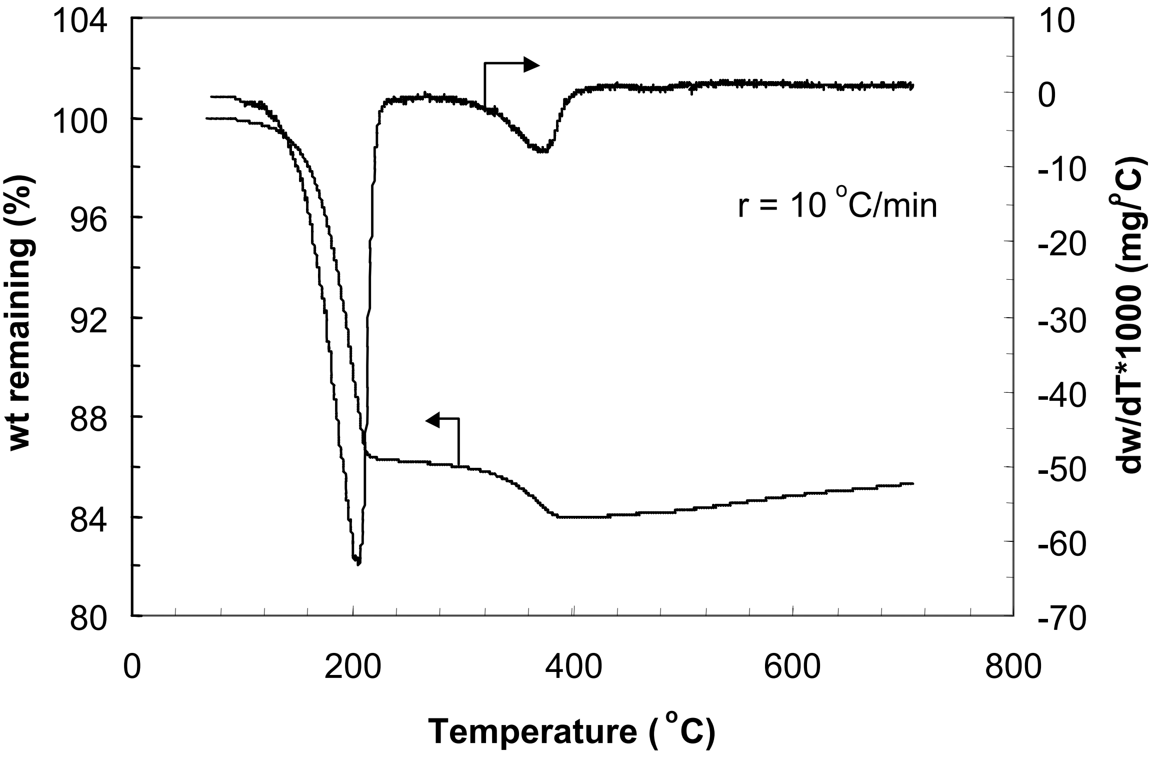

Figure 3. Thermo gravimetric analysis of an aqueous Co coated Ni tape

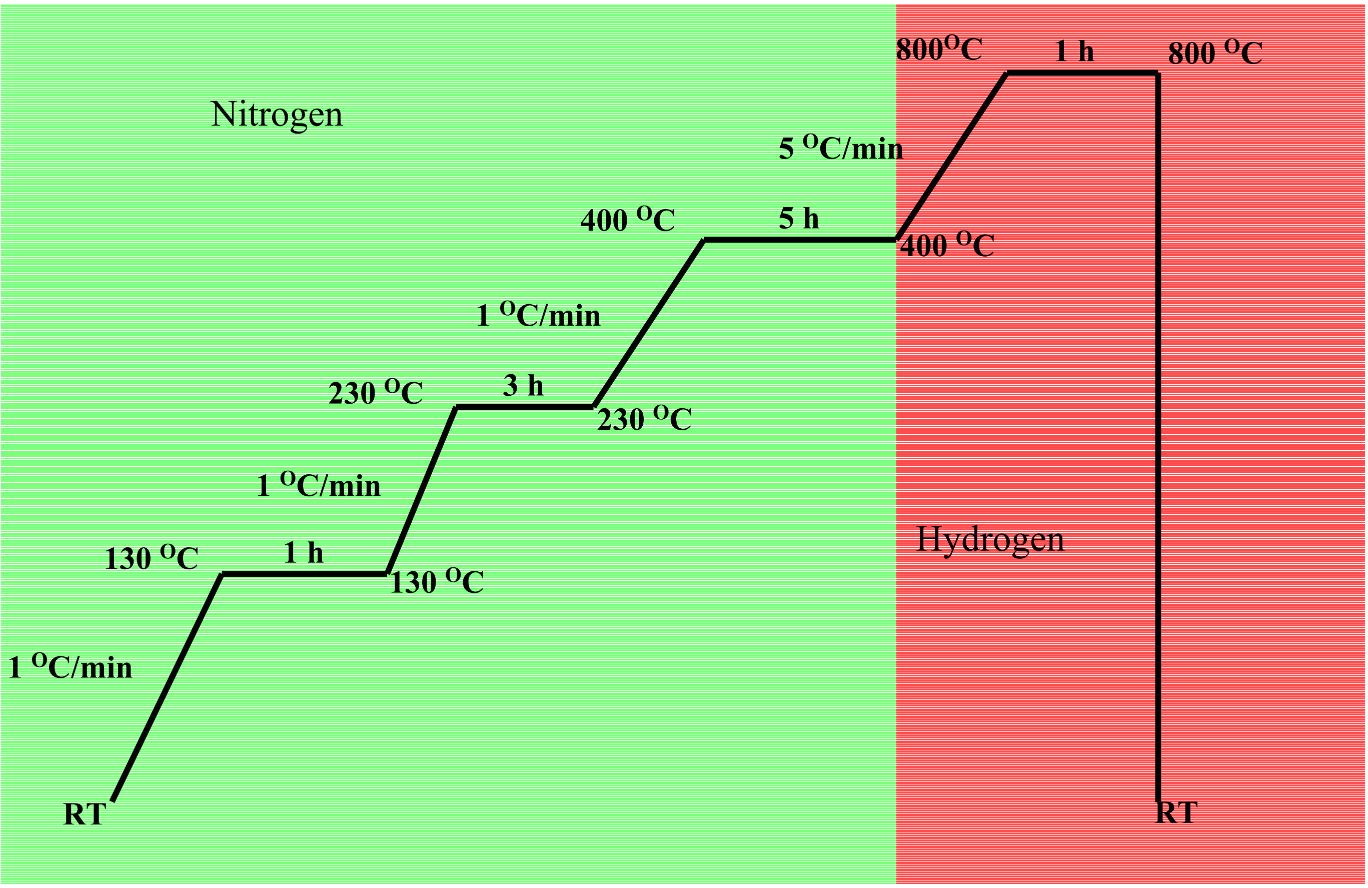

1 ^{O}C/min

Figure 4. Heating schedule for Co coated Ni green tapes

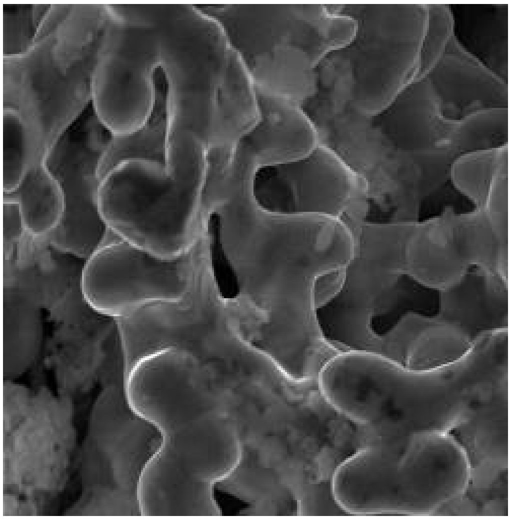

(a) Nickel Electrode Prepared by Aqueous Tapecasting

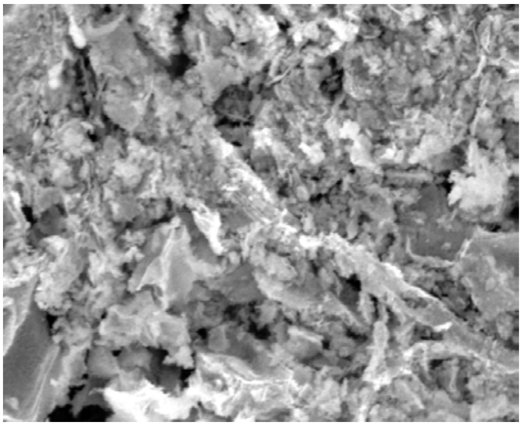

(b) Nickel Electrode after sol-gel coating

(c) Sol-gel coated Nickel Electrode after sintering at 700º C

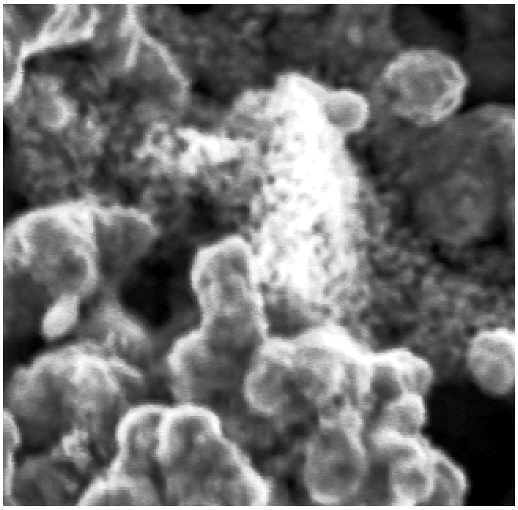

(d) PVA assisted Sol-gel coated Nickel Electrode after sintering at 700º C

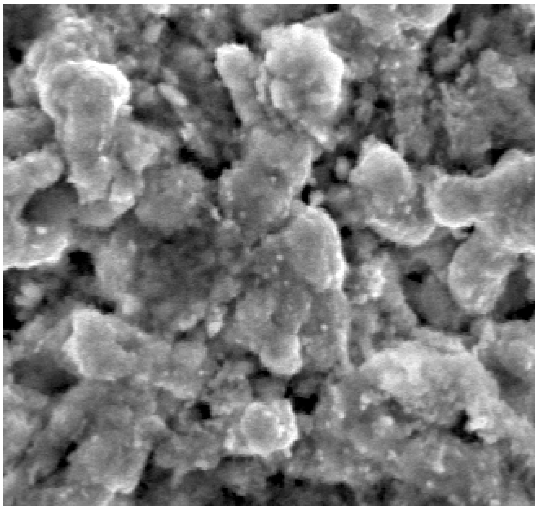

Figure 5. SEM images of Ni and lithium cobalt oxide coated nickel electrodes. Magnification of the electron micrographs is 2500.

Sol-Gel EDX Analysis

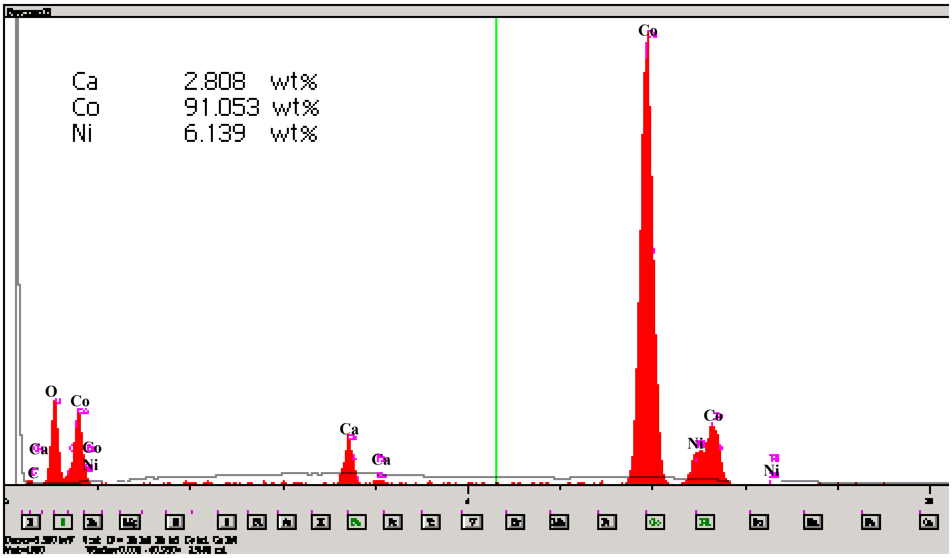

PVA asssisted Sol-Gel EDX Analysis

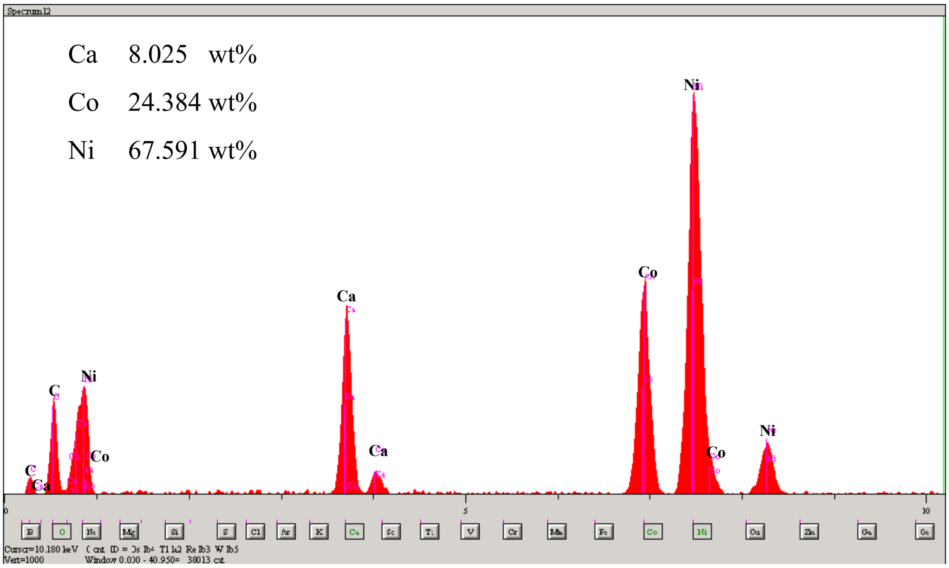

Figure 6. EDX analysis of lithium cobalt oxide coated nickel electrodes

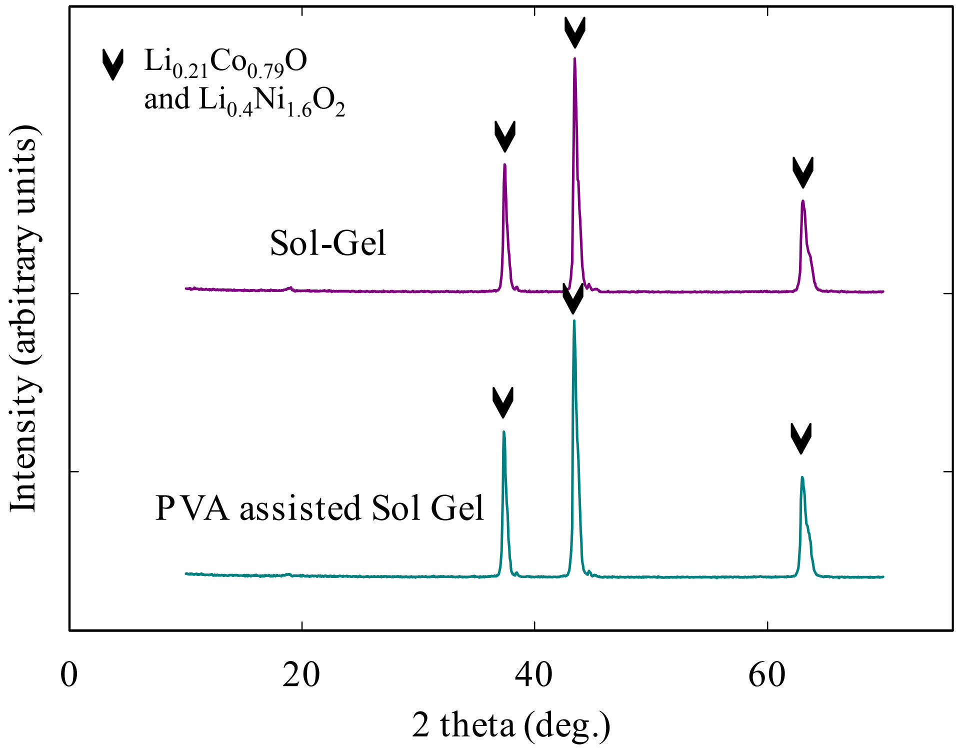

Figure 7. XRD analysis of lithium cobalt oxide coated nickel electrodes

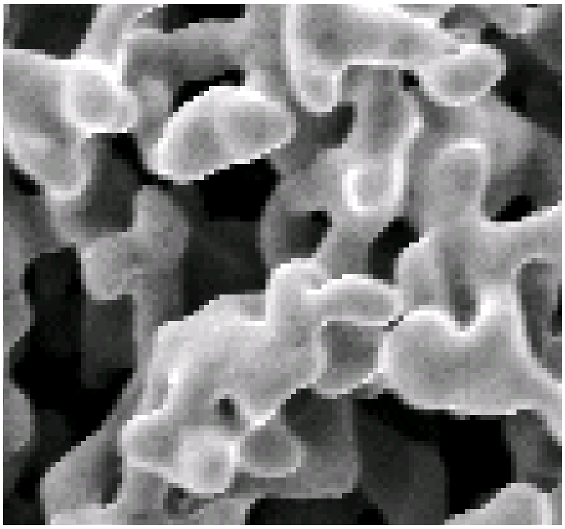

Figure 8. SEM image of cobalt coated nickel electrodes

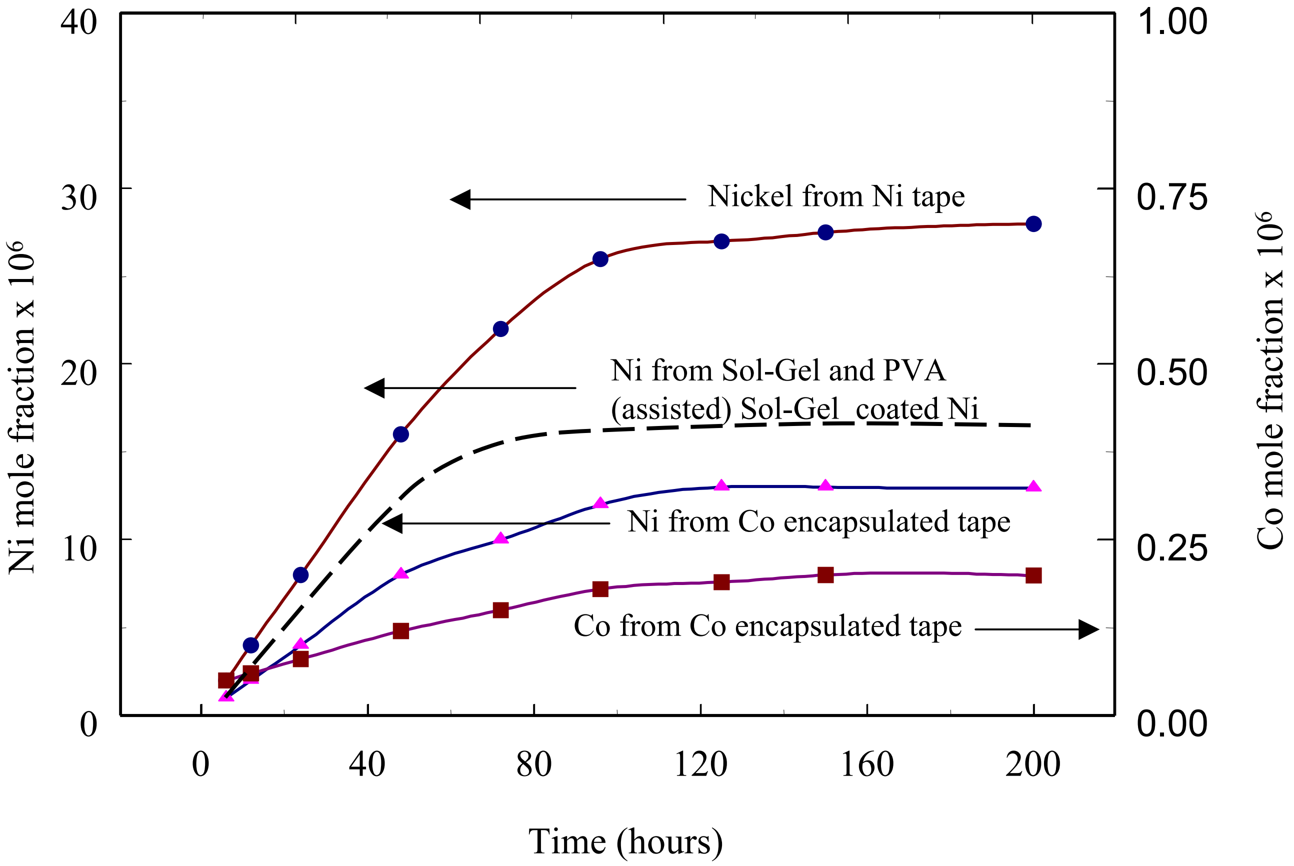

Figure 9. Dissolved nickel and cobalt in the carbonate melt as a function of time

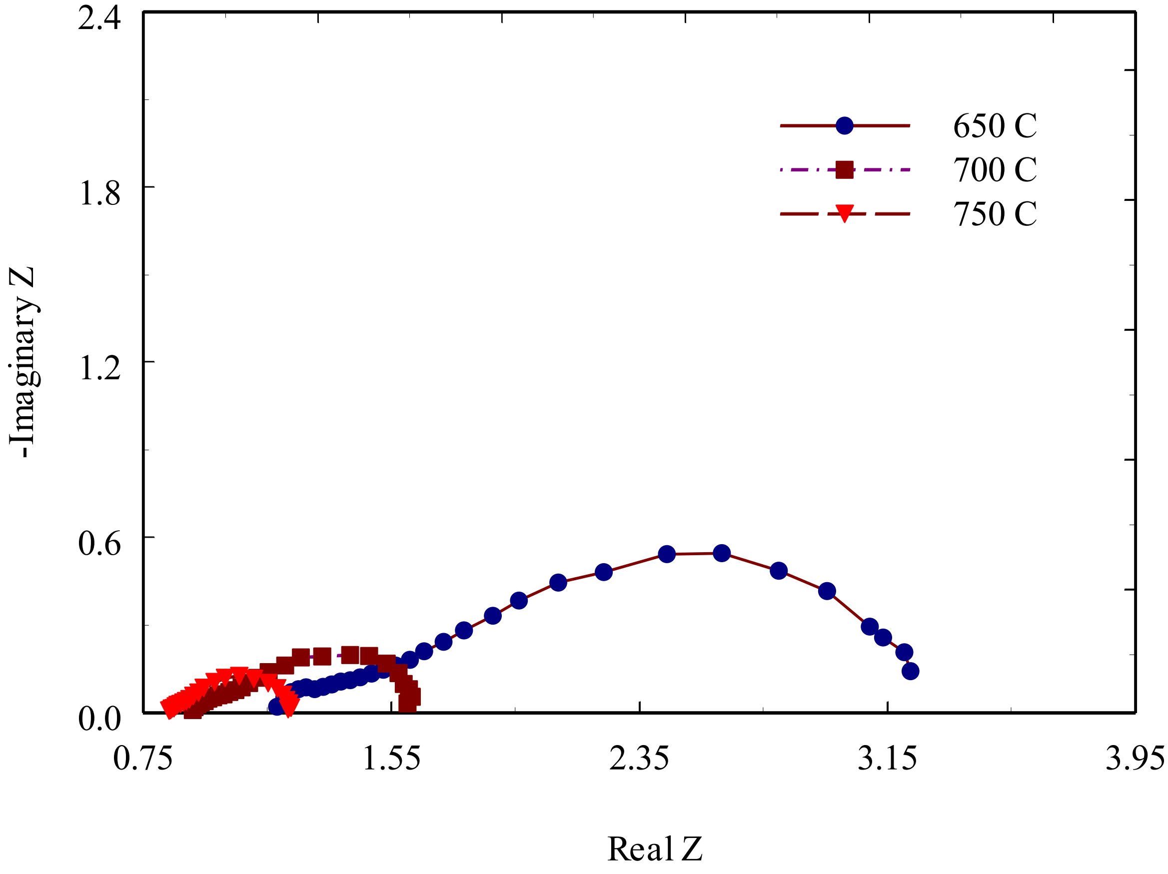

Figure 10. NiO impedance at 70 % air and 30 % CO_2

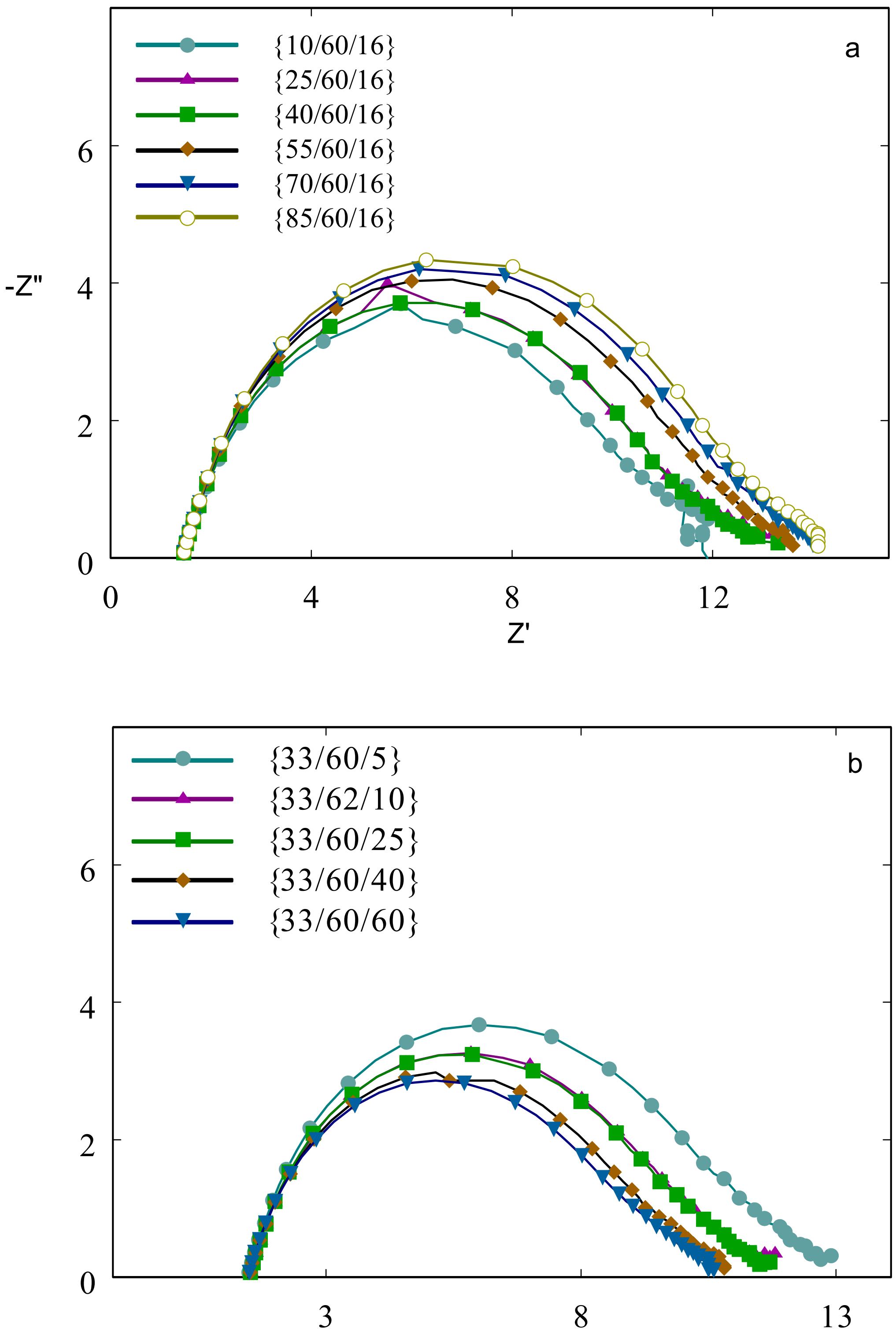

Figure 11. Impedance analysis varying (a) CO_2 partial pressure and (b)O_2 partial pressure

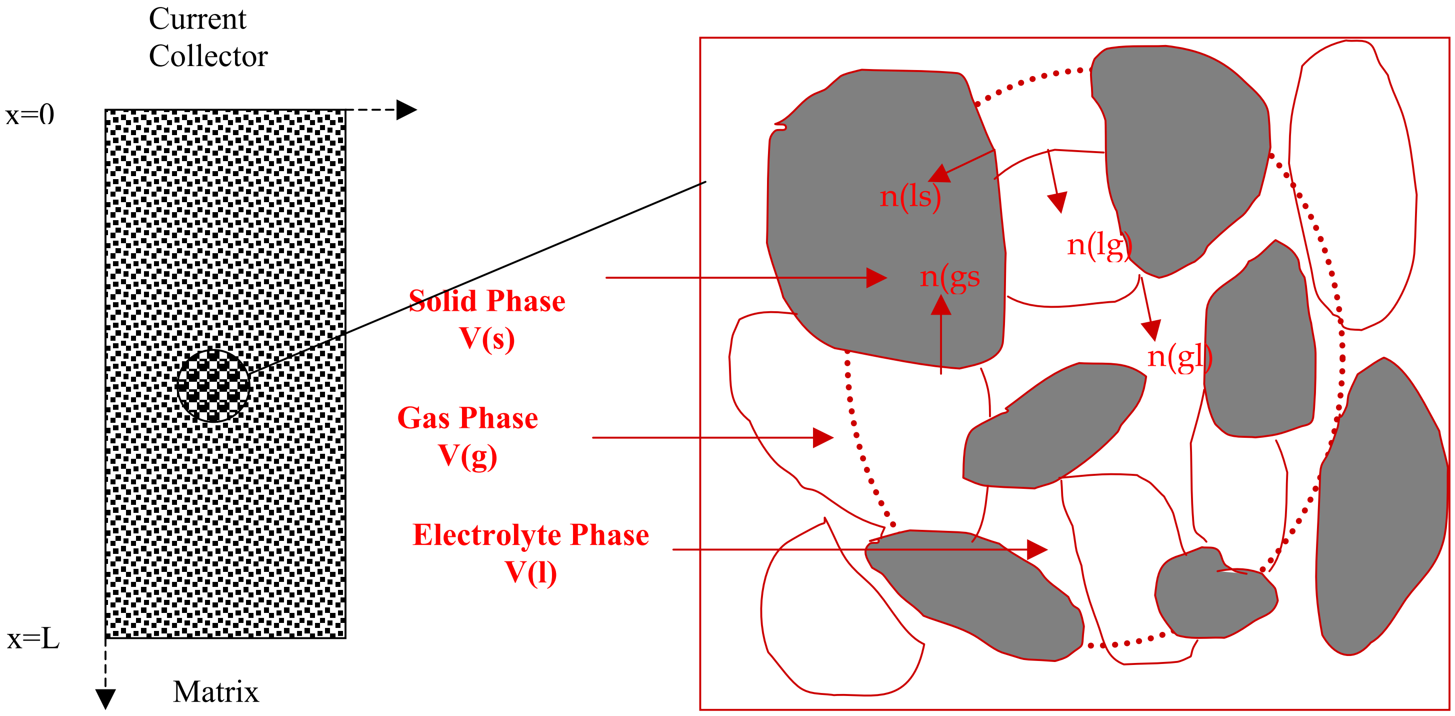

Figure 12. Volume averaging in porous electrode

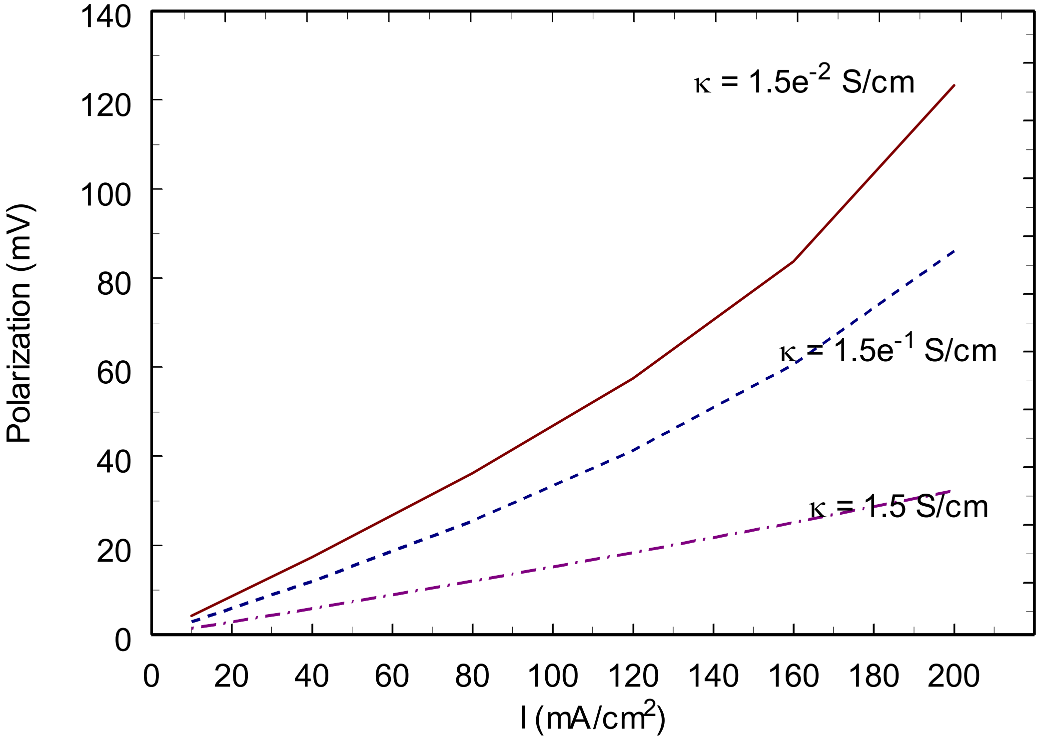

Figure 13. Effect of electrolyte conductivity

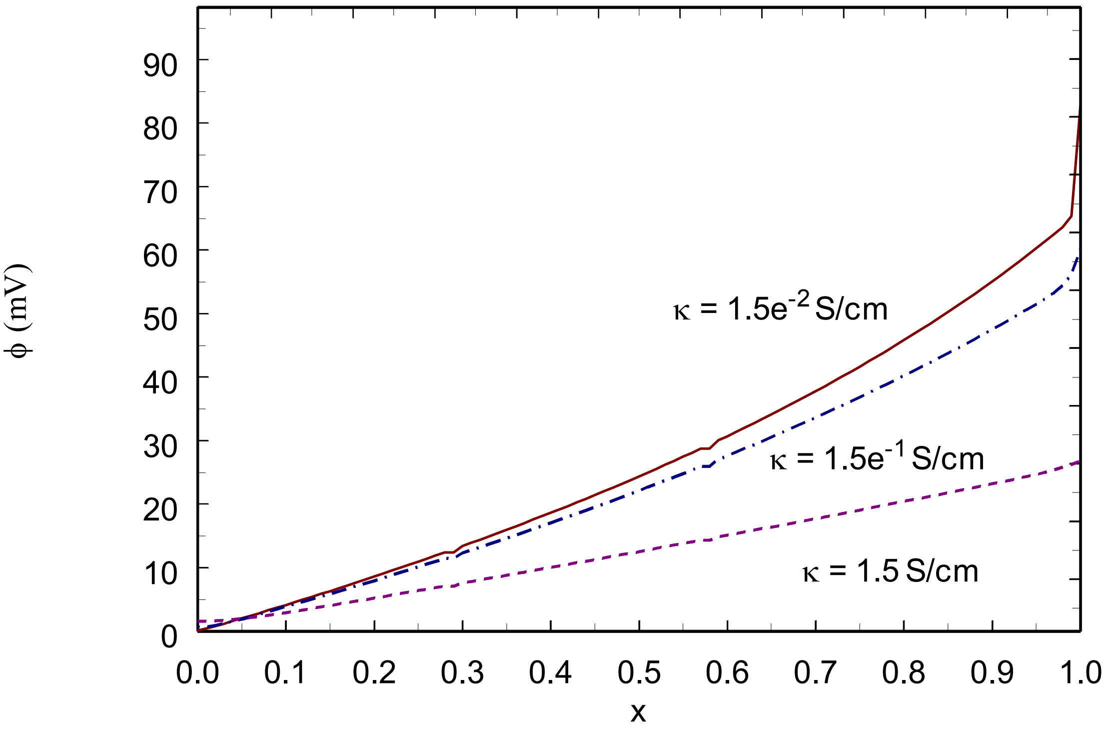

Figure 14. Comparison of overpotential profiles for varying electrolyte conductivity

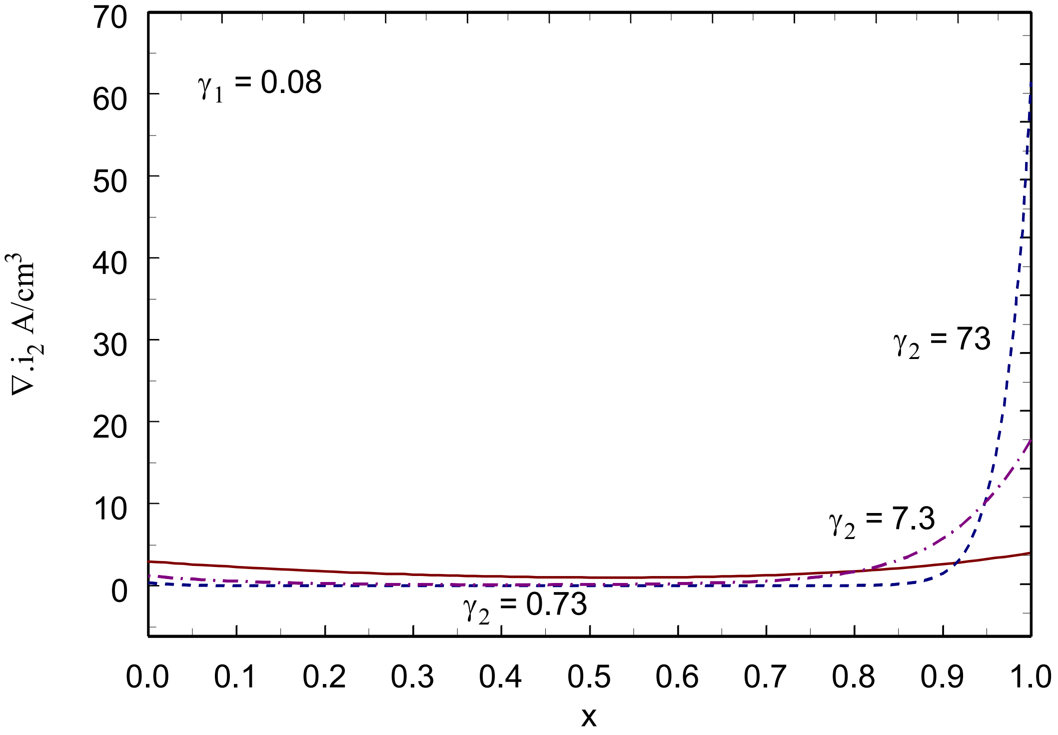

Figure 15. Comparison of reaction rate for varying electrolyte conductivity

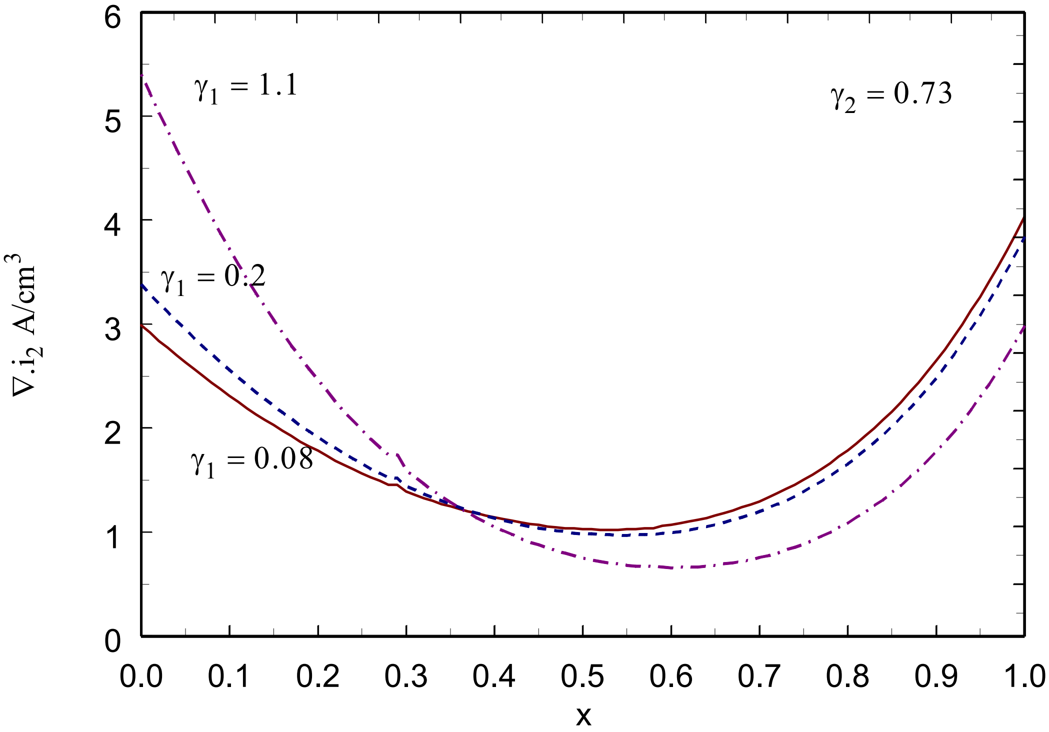

Figure 16. Comparison of reaction rate for varying electrode conductivity

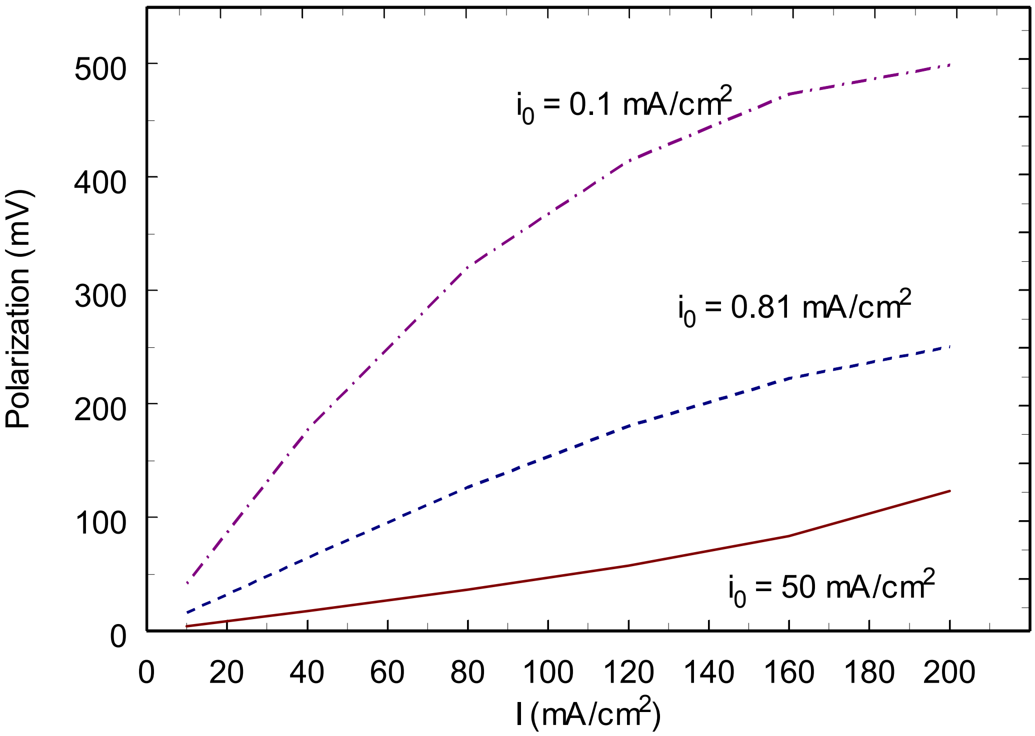

Figure 17. Effect of exchange current density

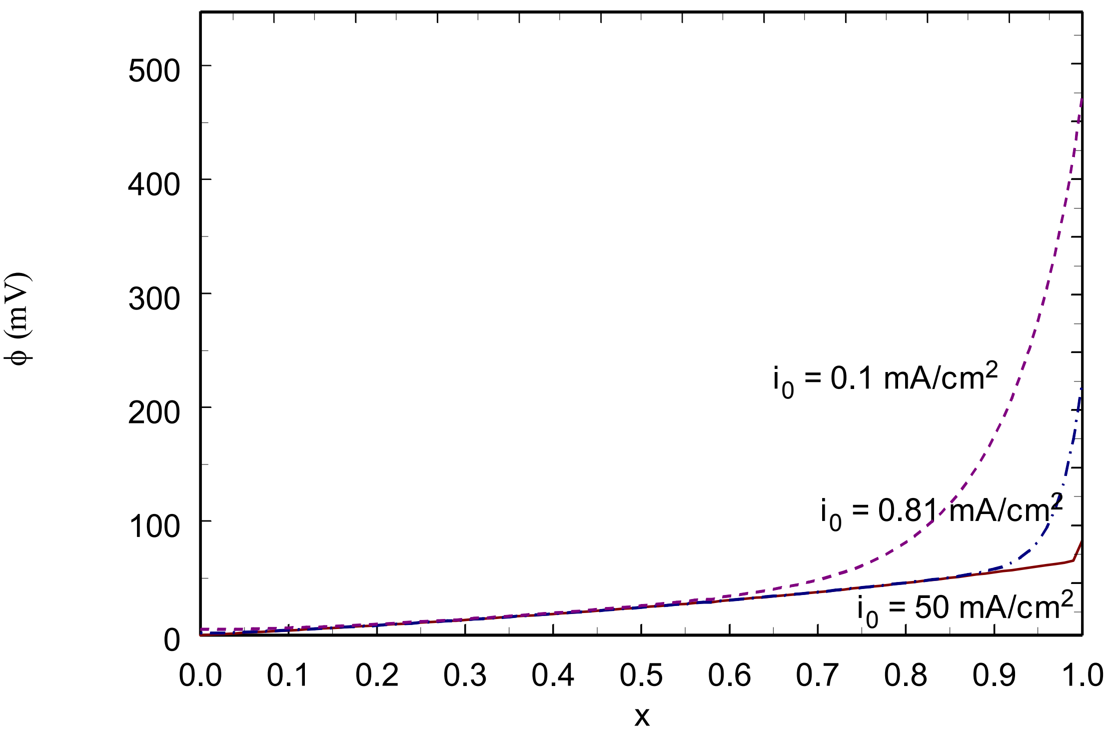

Figure 18. Comparison of overpotential profiles for varying exchange current density

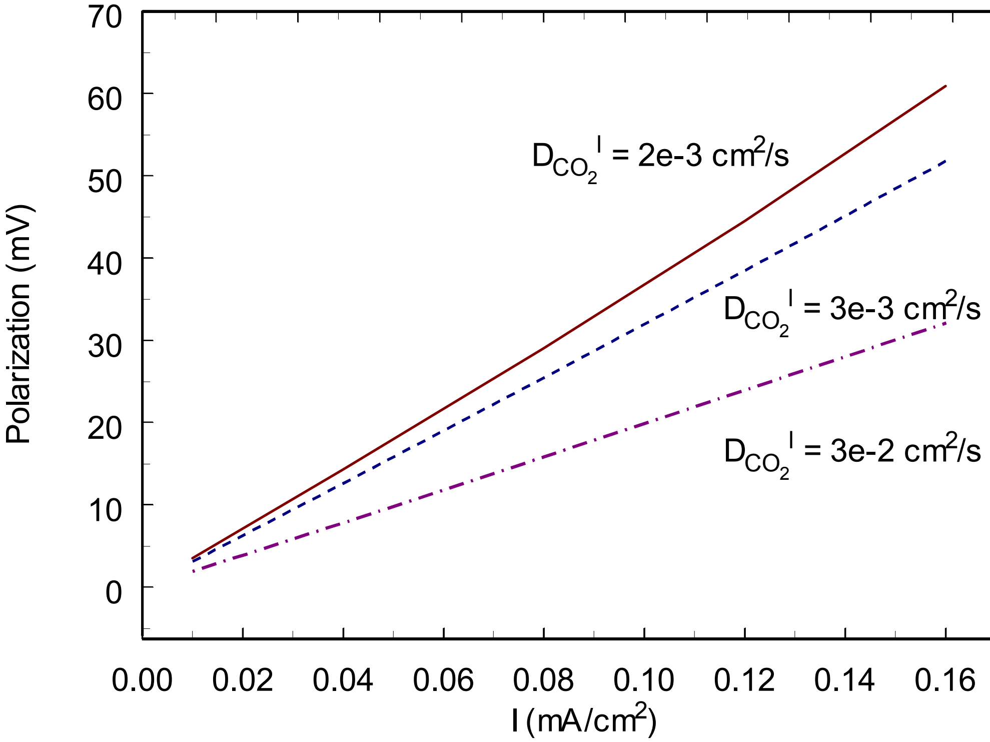

Figure 19. Effect of liquid phase diffusion coefficient of CO_2

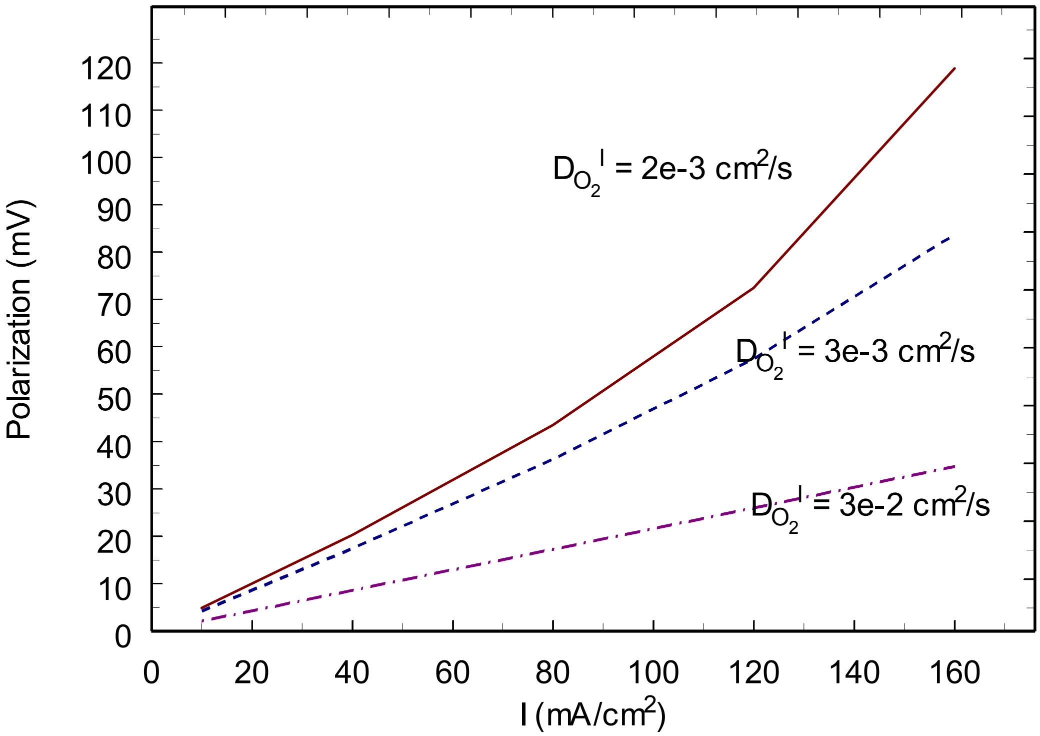

Figure 20. Effect of liquid phase diffusion coefficient of O_2

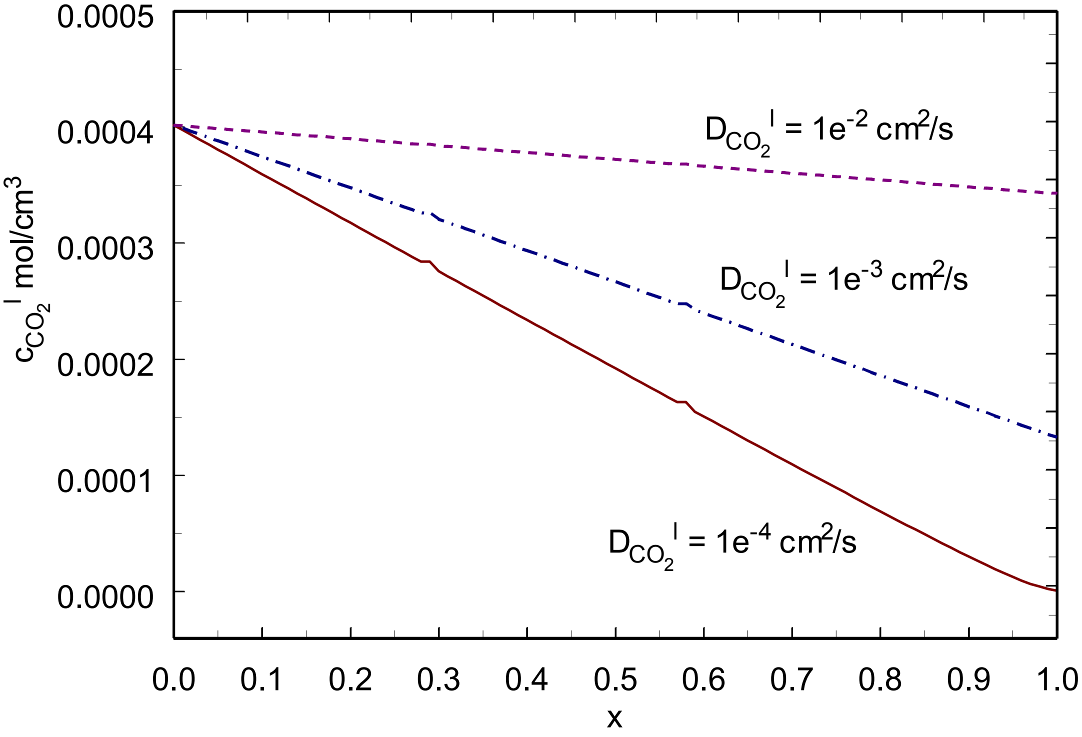

Figure 21. Comparison of concentration profiles for varying diffusion coefficient

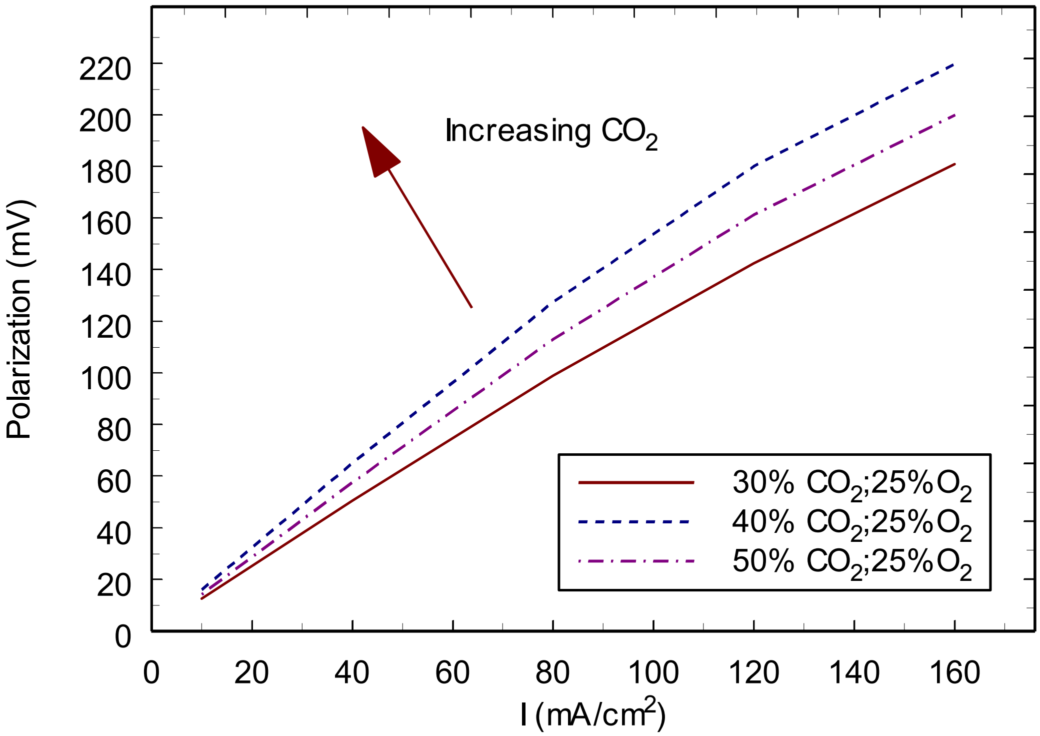

Figure 22. Effect of CO$_2$ gas composition

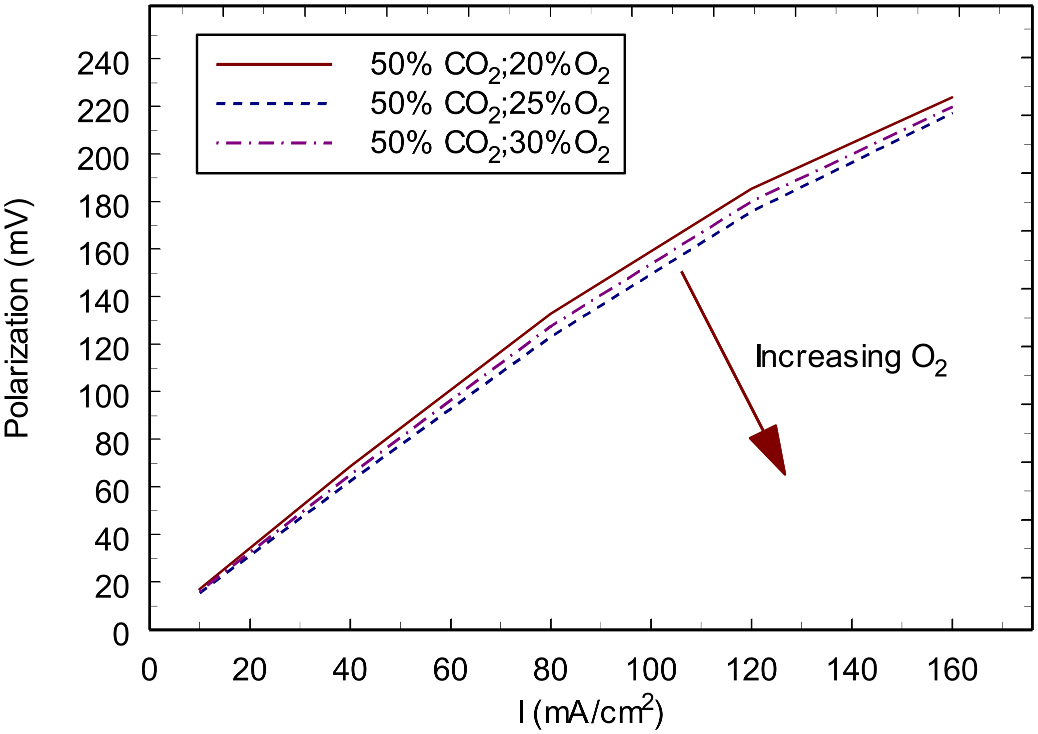

Figure 23. Effect of O_2 gas phase composition

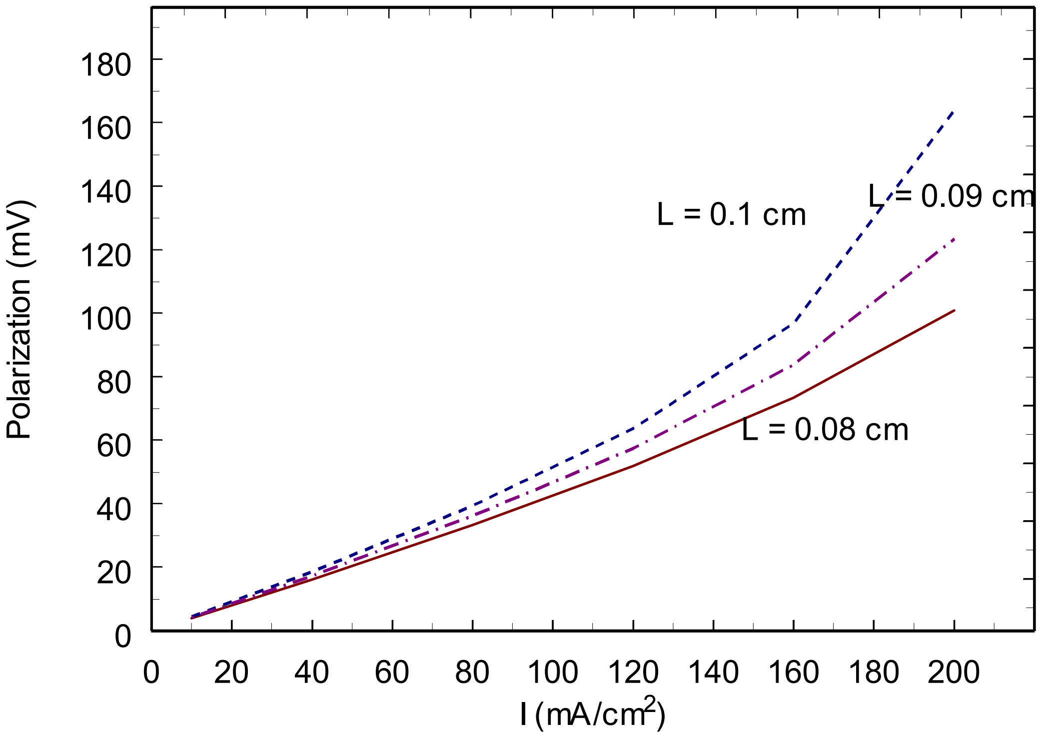

Figure 24. Effect of electrode thickness

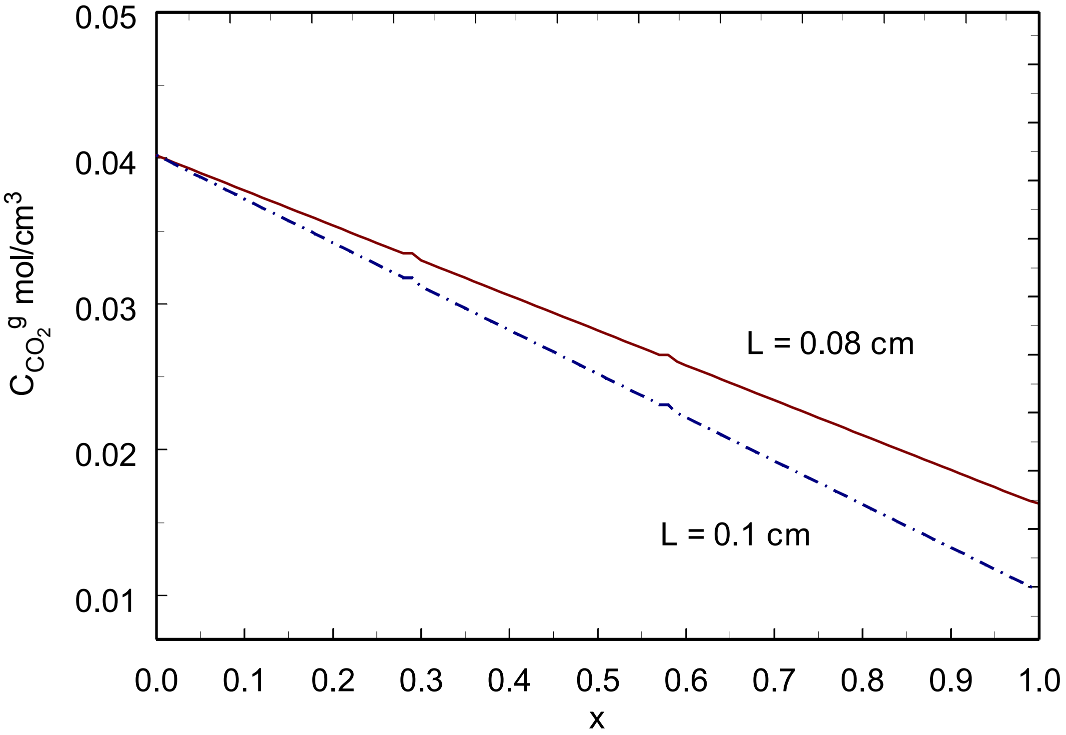

Figure 25. Comparison of concentration profiles in the gas phase for varying electrode thickness

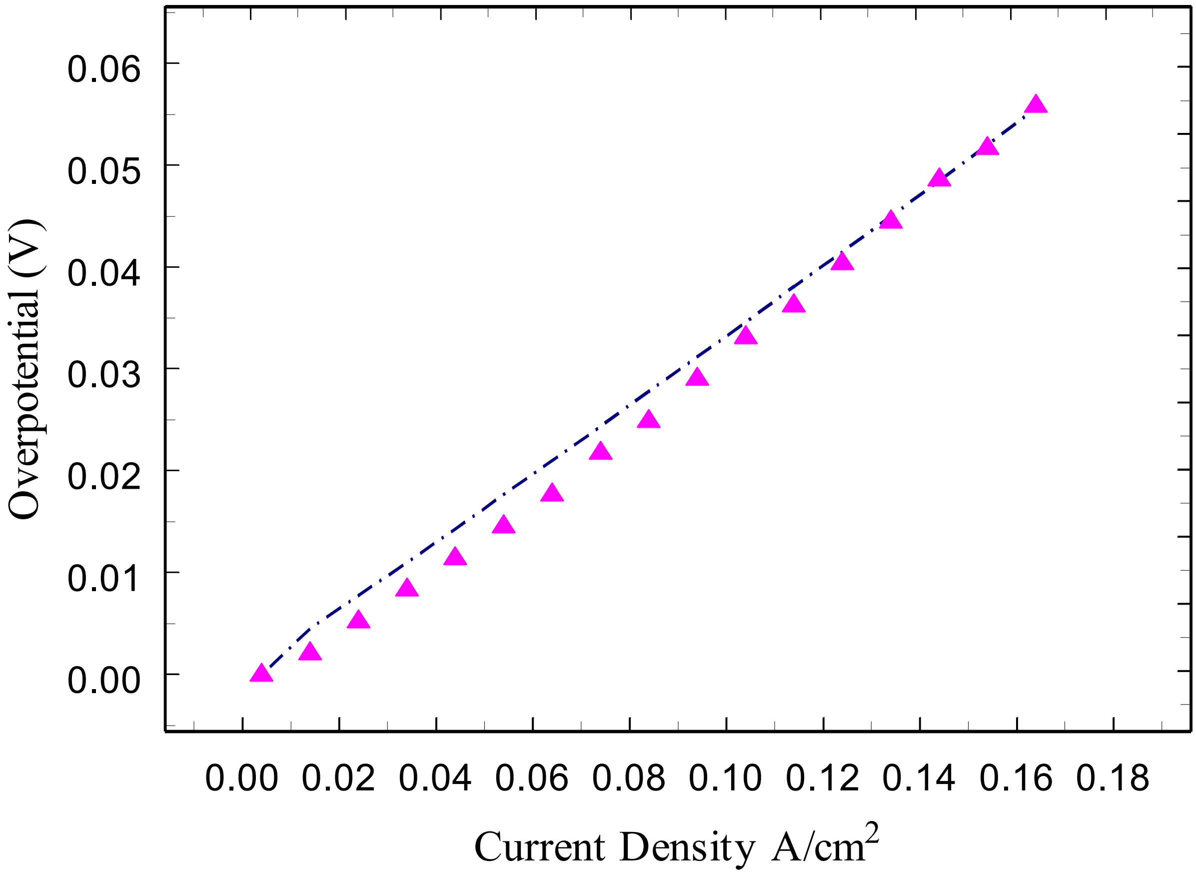

Figure 26. Comparison of experimental and model polarization data for the MCFC cathode.